CHALMERS

Chalmers Publication Library

DUst around NEarby Stars. The survey observational results

(article starts on next page)

Astronomy & Astrophysics

DUst around NEarby Stars. The survey observational results[*],[**],[***],[****]

C. Eiroa[1],[†], J. P. Marshall[1], A. Mora[2], B. Montesinos[3], O. Absil[4], J. Ch. Augereau[5], A. Bayo[6,7], G. Bryden[8],
W. Danchi[9], C. del Burgo[10], S. Ertel[5], M. Fridlund[11], A. M. Heras[11], A. V. Krivov[12], R. Launhardt[7], R. Liseau[13],
T. Löhne[12], J. Maldonado[1], G. L. Pilbratt[11], A. Roberge[9], J. Rodmann[14], J. Sanz-Forcada[3], E. Solano[3], K. Stapelfeldt[9],
P. Thébault[15], S. Wolf[16], D. Ardila[17], M. Arévalo[3,33], C. Beichmann[18], V. Faramaz[5], B. M. González-García[19],
R. Gutiérrez[3], J. Lebreton[5], R. Martínez-Arnáiz[20], G. Meeus[1], D. Montes[20], G. Olofsson[21], K. Y. L. Su[22],
G. J. White[23,24], D. Barrado[3,25], M. Fukagawa[26], E. Grün[27], I. Kamp[28], R. Lorente[29], A. Morbidelli[30], S. Müller[12],
H. Mutschke[12], T. Nakagawa[31], I. Ribas[32], and H. Walker[24]

(Affiliations can be found after the references)

ABSTRACT

Context. Debris discs are a consequence of the planet formation process and constitute the fingerprints of planetesimal systems. Their solar system counterparts are the asteroid and Edgeworth-Kuiper belts.
Aims. The DUNES survey aims at detecting extra-solar analogues to the Edgeworth-Kuiper belt around solar-type stars, putting in this way the solar system into context. The survey allows us to address some questions related to the prevalence and properties of planetesimal systems.
Methods. We used *Herschel*/PACS to observe a sample of nearby FGK stars. Data at 100 and 160 μm were obtained, complemented in some cases with observations at 70 μm, and at 250, 350 and 500 μm using SPIRE. The observing strategy was to integrate as deep as possible at 100 μm to detect the stellar photosphere.
Results. Debris discs have been detected at a fractional luminosity level down to several times that of the Edgeworth-Kuiper belt. The incidence rate of discs around the DUNES stars is increased from a rate of ~12.1% ± 5% before *Herschel* to ~20.2% ± 2%. A significant fraction (~52%) of the discs are resolved, which represents an enormous step ahead from the previously known resolved discs. Some stars are associated with faint far-IR excesses attributed to a new class of cold discs. Although it cannot be excluded that these excesses are produced by coincidental alignment of background galaxies, statistical arguments suggest that at least some of them are true debris discs. Some discs display peculiar SEDs with spectral indexes in the 70–160 μm range steeper than the Rayleigh-Jeans one. An analysis of the debris disc parameters suggests that a decrease might exist of the mean black body radius from the F-type to the K-type stars. In addition, a weak trend is suggested for a correlation of disc sizes and an anticorrelation of disc temperatures with the stellar age.

Key words. circumstellar matter – planetary systems – infrared: stars

1. Introduction

Circumstellar discs are formed around stars as a by-product required by angular momentum conservation. In their earliest phases, stars accrete a significant part of their masses from gas and dust in the discs. Meanwhile, those circumstellar accretion discs evolve from a gas-dominated protoplanetary phase to a gas-poor debris-disc phase where large planetesimals and full-sized planets may have formed, after primordial submicron-sized dust grains settle in the disc midplane and coagulate to form dust aggregates, pebbles, and larger rocky bodies. Most likely this is the formation pathway followed by the currently

known exoplanets (close to one thousand) and our own solar system to form. However, it is not known which are the ultimate circumstances and physical conditions that make planet formation possible, and whether planet formation is nearly as universal during disc evolution as is the formation of discs during star formation. This issue is central to understand the incidence of planetary systems in general, and consequently the formation of Earth-like planets.

In the solar system, the planets together with asteroids, comets, the zodiacal material and the Edgeworth-Kuiper belt (EKB) are the fingerprints of such dynamical processes. Planet formation resulted in a nearly total depletion of planetesimals inside the orbit of Neptune, with the remarkable exception of the asteroid belt. Leftover planetesimals not incorporated into planets arranged to form the EKB, beyond the orbit of Neptune, dynamically sculpted and excited by the giant planets. Mutual collisions between EKB objects and erosion by interstellar dust grains release dust particles that spread over the EKB region (Jewitt et al. 2009). If the EKB could be observed from afar, it would appear as an extended (~50 AU) and very faint ($L_d/L_\odot \sim 10^{-7}$) emission with a temperature of 70–100 K (Backman et al. 1995; Vitense et al. 2010, 2012), with a huge central hole caused by the massive planets (Moro-Martín & Malhotra 2005).

The discovery of IR excesses in main-sequence stars such as Vega, Fomalhaut or β Pic was one of the most significant accomplishments of the IRAS satellite (Aumann et al. 1984). The observed excess was attributed to thermal emission from solid particles around the stars. Optical imaging of β Pic convincingly demonstrated that the dust was located in a flattened circumstellar disc (Smith & Terrile 1984). Since lifetimes of dust grains against radiative/wind removal, Poynting-Robertson drag and collisional disruption are much shorter than the age of the stars, one must conclude that these dust particles are not remnants of the primordial discs, instead they are the result of ongoing processes. Nearly all modelling efforts explain "debris discs" dust production as a result of collisions of larger bodies (Wyatt 2008; Krivov 2010, and references therein). Given that debris discs survive over billions of years, there must be a large reservoir of leftover planetesimals and solid bodies that collide and are intimately related to the dust particles. Furthermore, dust particles respond in different ways to the gravity of planetary perturbers depending on their size distribution and can be used as a tracer of planets (Augereau et al. 2001; Quillen & Thorndike 2002; Moro-Martín et al. 2007; Mustill & Wyatt 2009; Thebault et al. 2012). Consequently, observations of debris discs shed light onto the processes related to planet and planetesimal formation.

Much observational as well as modelling progress has occurred in the last two decades primarily from infrared (IR) and (sub)-millimetre facilities. The first debris discs were discovered by the InfraRed Astronomical Satellite (IRAS), mainly around A stars due to sensitivity limitations. The Infrared Space Observatory (ISO) extended the study of debris discs and added important information on the age distribution of debris discs (Habing et al. 2001). More recently, *Spitzer* added a wealth of new information in a variety of aspects. For example, the incidence rate was found to be larger for A stars and then it decreased with later spectral types up to M stars (Su et al. 2006; Gautier et al. 2007). An incident rate of ~16% was found around solar-type FGK stars (Trilling et al. 2008), not dependent on the stellar metallicity (Beichman et al. 2006), although a marginal trend might exist, as recently suggested by Maldonado et al. (2012). The presence of exoplanets is not necessarily a sign for a higher incidence of debris discs (Kóspál et al. 2009), although Wyatt et al. (2012) have recently claimed that the debris incidence rate is higher around stars with low mass planets, and there may be trends between some debris discs and planet properties when both simultaneously exist (Maldonado et al. 2012). *Spitzer* also found that typical debris discs around solar-type stars emit much stronger at 70 μm than at 24 μm, with the detection rate for hot discs being very low. Spectral energy distributions (SEDs) imply the dust is located at several tens of AU and dust temperatures ~50–150 K (Trilling et al. 2008; Moór et al. 2011). However, the distance, dust mass and optical properties are degenerate with the (unknown) particle size distribution.

In spite of its remarkable contribution *Spitzer* suffered from two severe constraints. Firstly, its moderate sensitivity, $L_{\rm d}/L_{\star} \sim 10^{-5}$ (Trilling et al. 2008), i.e., about two orders of magnitude above the EKB luminosity, and its wavelength coverage, in practice up to 70 μm, limited its ability to detect cold dust. Secondly, its moderate spatial resolution prevented detailed studies of the spatial structure in debris discs since it resolved only a few discs. Significantly higher spatial resolution is required in order to determine the location of the dust and its spatial distribution, which traces rings, warps, cavities, or asymmetries, and which can be used to infer the potential presence of planets (Mouillet et al. 1997; Lagrange et al. 2010). The ESA *Herschel* Space Telescope (Pilbratt et al. 2010) overcomes these limitations thanks to its

larger mirror and instruments PACS (Poglitsch et al. 2010) and SPIRE (Griffin et al. 2010), which allow for a better sensitivity, wavelength coverage and higher spatial resolution.

In this paper we summarize the observational results obtained in the frame of the *Herschel* open time key programme DUNES[1], DUst around NEarby Stars (KPOT_ceiroa_1 and SDP_ceiroa_3). This programme aims at detecting EKB analogues around nearby solar-type stars; putting in this manner the solar system into context. The content of this paper addresses the DUNES observational results presented as a whole. Detailed analysis or studies of individual sources or groups of objects are out of the scope of this work. For such more detailed and deeper studies we refer to some already published observational (Liseau et al. 2010; Eiroa et al. 2010, 2011; Marshall et al. 2011), and modelling papers (Ertel et al. 2012a; Löhne et al. 2012), as well as to forthcoming ones. The current paper is organized as follows: Sect. 2 describes the scientific rationale and the observing strategy. Section 3 presents the sample of stars. Section 4 describes the *Herschel* PACS and SPIRE observations and data reduction, while the treatment of PACS noise and the results are presented in Sects. 5 and 6, respectively. The analysis of the data of the non-excess sources with the upper limits of the fractional luminosity of the dust are in Sect. 7.1. The detected debris discs are presented in Sect. 7.2, where the background contamination and some general properties and characteristics of the discs are described. Section 8 presents a discussion of disc properties and some stellar parameters. Finally, Sect. 9 contains a summary and our conclusions. In addition, several appendixes give some fundamental parameters of the stars, the method used for the photospheric fits, and a short description of some spurious objects.

2. DUNES Scientific objectives: Survey rationale

The primary scientific objective of DUNES is the identification and characterization of faint exosolar analogues to the solar system EKB in an unbiased sample of nearby solar-type stars. Strictly speaking, the detection of such faint discs is a direct proof of the incidence of planetesimal systems and an indirect one of the presence planets. The survey design allows us to additionally address several fundamental, specific questions that help to evaluate the prevalence and properties of such planetesimal and planetary systems. These are: i) the fraction of solar-type stars with faint, EKB-like discs; ii) the collisional and dynamical evolution of EKB analogues; iii) the dust properties and size distribution; and iv) the incidence of EKB-like discs versus the presence of planets.

According to the recent EKB model of Vitense et al. (2012), the predicted infrared excess peaks at ~50 μm and the flux levels in the PACS bands would be between 0.1 and 0.4 mJy. This flux is about an order of magnitude lower than the expected photospheric fluxes from nearby solar-type stars (see Appendix C), and few times lower than the predicted pre-launch sensitivity of PACS (PACS observer's manual, version 1.3, 04/July/2007). Therefore, the challenge of detecting a faint infrared excess, which could be considered as an exo-EKB analogue, is the detection of a faint far-IR signal from a debris disc on top of a weak photospheric signal which is few times the expected measurement uncertainties.

The observing strategy is also modulated by the choice of the optimal wavelength. The equilibrium temperature of a dust grain depends on the stellar luminosity, the radial distance to
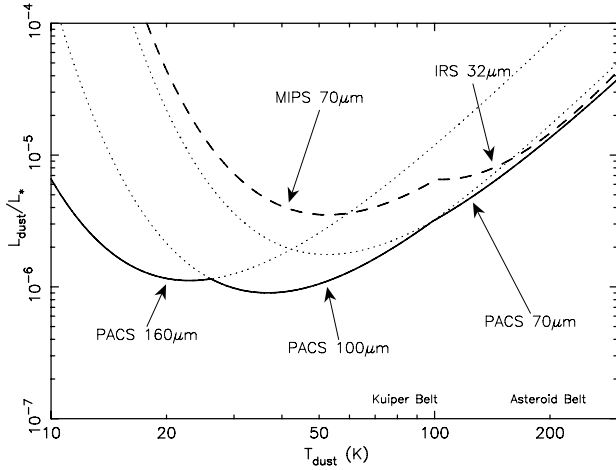
---

[1] http://www.mpia-hd.mpg.de/DUNES/

Fig. 1. Detection limits for a G2V star at 10 pc for the *Herschel* 70, 100, and 160 μm bands compared to the *Spitzer* instruments MIPS at 70 μm and IRS at 32 μm.

Table 1. Summary of spectral types in the DUNES sample and the shared sources observed by DEBRIS.

Sample	F stars	G stars	K stars	Total
Solar-type stars observed by				
DUNES (the DUNES sample)	27	52	54	133
20 pc DUNES subsample	20	50	54	124
Shared solar-type stars				
observed by Debris	51	24	8	83
Shared 20 pc subsample	32	16	8	56

the star, and dust properties (size, chemical composition, mineralogy). For distances of ~30–100 AU, grains of about 10 μm in size have temperatures in the range ~30–50 K (Krivov et al. 2008). At these temperatures, the bulk of the thermal re-emission is radiated in the far-IR covered by the PACS photometric bands centered at 70, 100, and 160 μm. Figure 1 highlights the unique *Herschel* PACS discovery space compared to *Spitzer* MIPS and IRS. The limits in Fig. 1 are calculated assuming PACS 1σ accuracies of 1.5, 1.5, and 3.5 mJy at 70, 100, and 160 μm, respectively. A systematic uncertainty of 5% is also included for calibration uncertainty. Note that these accuracies are larger than the typical uncertainties found in this survey (e.g. Table 12), and that the systematic uncertainty is larger than that reported in the PACS technical note PICC-ME-TN-037[2]. *Spitzer*/MIPS limits are based on an assumed photometry accuracy of 3 mJy and a 10% systematic contribution (e.g. Bryden et al. 2009). *Spitzer*/IRS is limited to a 2% uncertainty at 32 μm (Lawler et al. 2009). The assumed photospheric uncertainty for both PACS and MIPS is 2%. The plot shows in particular that PACS 100 μm provides the most suitable range to detect very faint discs for dust temperatures in the range from ~20 to ~100 K. Further, with a detection limit of $L_{\rm d}/L_{\star}$ few times 10^{-7}, PACS 100 μm has the ability to reveal dust discs with emission levels close to the EKB. We note that although the PACS 70 μm band has a sensitivity similar to PACS 100 μm for EKB temperatures around 100 K, and is more competitive in terms of background confusion and stellar photospheric detection, 100 μm provides a better contrast ratio between the emission of cold dust and the stellar photosphere, and is in fact much more sensitive than PACS 70 μm for probing very faint, cold discs.

Given the above considerations concerning flux levels from the EKB analogues and the stars together with the optimal wavelength, the choice to fulfil the DUNES objectives was to integrate as deep as needed to achieve the estimated photospheric flux levels at 100 μm.

3. The stellar sample

The preliminary stellar sample was chosen from the HIPPARCOS catalogue (ESA 1997) following the sole criterion of selecting main-sequence, luminosity classes V-IV/V, stars closer than

---

[2] Technical note in http://herschel.esac.esa.int

25 pc without any further bias concerning any property of the stars. Since the *Herschel* observations were designed to detect the photosphere, the only restriction to build the final sample was that the stars could effectively be detected by PACS at 100 μm with a $S/N \geq 5$, i.e., the expected 100 μm photospheric flux should be significantly higher than the expected background as estimated by the *Herschel* HSPOT tool at that wavelength. Taking into account the total observing time finally allocated for the DUNES survey (140 h) as well as the complementarity with the *Herschel* OTKP DEBRIS (Matthews et al. 2010), the stellar sample for this study was reduced to main-sequence FGK solar-type stars located at distances smaller than 20 pc. In addition, from the original sample we retained FGK stars between 20 and 25 pc hosting exoplanets (3 stars, 1 F-type and 2 G-type, at the time of the proposal writing) and previously known debris discs, mainly from the *Spitzer* space telescope (6 stars, all F-type). Thus, the final sample of stars directly observed by DUNES, formally called the DUNES sample in this paper, is formed by 133 stars, 27 out of which are F-type, 52 G-type, and 54 K-type stars. The 20 pc subsample is formed by 124 stars – 20 F-type, 50 G-type and 54 K-type. Table 1 summarizes the spectral type distribution of the samples.

The OTKP DEBRIS project was defined as a volume limited study of A through M stars selected from the "UNS" survey (Phillips et al. 2010), observing each star to an uniform depth, i.e., DEBRIS is a flux-limited survey. In order to optimize the results according to the DUNES and DEBRIS scientific goals, the complementarity of both surveys was achieved by dividing the common stars of both original samples considering if the stellar photosphere could be detected with the DEBRIS uniform integration time. Those stars were assigned to be observed by DEBRIS. In that way, the DUNES observational objective of detecting the stellar photosphere was satisfied. The few A-type and M-type stars common in both surveys were also assigned to DEBRIS.

The net result of this exercise was that 106 stars observed by DEBRIS satisfy the DUNES photospheric detection condition and are, therefore, shared targets. Specifically, this sample comprises 83 FGK stars – 51 F-type, 24 G-type and 8 K-type (the rest are A and M stars). Since the assignment to one of the teams was made on the basis of both DUNES and DEBRIS original samples, the number of shared targets located closer than 20 pc, i.e., the revised DUNES distance, are less: 56 FGK – 32 F-type, 16 G-type, and 8 K-type stars (see Table 1). Considering HIPPARCOS completeness, the total sample – DUNES stars plus the shared stars observed by DEBRIS – should be fairly complete (with the constraint that the photosphere is detected with a $S/N \geq 5$ at 100 μm) up to the distance of 20 pc for the F and G stars, while it is most likely incomplete for distances larger than around 15 pc for the K-type stars, particularly for the latest K spectral types. We point out that because of the imposed condition of a photospheric detection over

Table 2. The DUNES stellar sample.

HIP	HD	Name	SpT	SpT range	ICRS (2000)	Galactic	π(mas)	d(pc)
171	224930	HR 9088	G3V	G2V – G5V	00 02 10.156 +27 04 56.13	109.6056 –34.5113	82.17 ± 2.23	12.17
544	166	V439 And	K0V	G8V – K0V	00 06 36.785 +29 01 17.40	111.2636 –32.8326	73.15 ± 0.56	13.67
910	693	6 Cet	F5V	F5V – F8V	00 11 15.858 –15 28 04.73	082.2269 –75.0650	53.34 ± 0.64	18.75
2941	3443	HR 159	K1V+...	G7V – G8V	00 37 20.720 –24 46 02.18	068.8453 –86.0493	64.93 ± 1.85	15.40
3093	3651	54 Psc	K0V	K0V – K2V	00 39 21.806 +21 15 01.71	119.1726 –41.5331	90.42 ± 0.32	11.06

Notes. Columns correspond to the following: HIPPARCOS and HD numbers as well as usual stars' names; spectral types and ranges (see text); equatorial and galactic coordinates; parallaxes with errors and stars' distances. Only the first 5 lines of the table are presented here. The full version is available at the CDS.

Table 3. Photometric magnitudes and fluxes of the DUNES stars.

HIP	V	$B-V$	$V-I$	$b-y$	m_1	c_1	J	H	K_s	Q
171	5.80	0.69	0.82	0.432	0.184	0.218	4.702 ± 0.214	4.179 ± 0.198	4.068 ± 0.236	CCD
544	6.07	0.75	0.80	0.460	0.290	0.311	4.733 ± 0.019	4.629 ± 0.144	4.314 ± 0.042	EBE
910	4.89	0.49	0.59	0.328	0.130	0.405	4.153 ± 0.268	3.800 ± 0.208	3.821 ± 0.218	DCD
2941	5.57	0.72	0.78	0.435	0.254	0.287	4.437 ± 0.266	3.976 ± 0.224	4.027 ± 0.210	DDC
3093	5.88	0.85	0.83	0.507	0.384	0.335	4.549 ± 0.206	4.064 ± 0.240	3.999 ± 0.036	CDE

Notes. Only the first 5 lines with the optical (Johnson and Strömgrem) and 2MASS photometry are shown here (see Appendixes B and C). The full version of the table including further near-IR data, AKARI, WISE, IRAS and *Spitzer* MIPS is available at the CDS.

Table 4. Fundamental stellar parameters and some properties of the DUNES sources (see Appendix B).

HIP	SpT	$T_{\rm eff}$ (K)	$\log g$ (cm/s^2)	[Fe/H] (dex)	$v \sin i$ (km s^{-1})	$L_{\rm bol}$ ($L_\odot$)	$L_{\rm x}/L_{\rm bol}$ (log)	AgeX (Gyr)	$\log R'_{\rm HK}$	Age(Ca II) (Gyr)
171	G3V	5681	4.86	–0.52	1.8	0.614	–5.9	3.12	–4.851	3.96
544	K0V	5577	4.58	0.12	3.4	0.616	–4.4	0.32	–4.328	0.17
910	F5V	6160	4.01	–0.38	3.8	3.151	–7.6	12.53	–4.788	3.04
2941	K1V+...	5509	4.23	–0.14	1.6:	1.258			–4.903	4.83
3093	K0V	5204	4.45	0.16	1.15	0.529	–6.0	4.53	–4.991	6.43

Notes. Only the first 5 lines are shown. The full version of the table is available at the CDS.

the background with $S/N > 5$ the number of "rejected sources" sources according to the HIPPARCOS catalogue are 10 F-type, 43 G-type, and 213 K-type stars.

Table 2 provides some basic information on the 133 stars in the DUNES sample. Columns 1 and 2 give HIPPARCOS and HD numbers, respectively, while Col. 3 gives the stars' names as provided by SIMBAD. HIPPARCOS spectral types are given in Col. 4; in order to check the consistency of these spectral types we have explored VIZIER using the DUNES discovery tool[3] (Appendix A). Results of this exploration are summarized in Col. 5 which gives the spectral type range of each star taken into account SIMBAD, Gray et al. (2003, 2006), Wright et al. (2003) and the compilation made by Skiff (2009). Typical spectral type range is 2–3 subtypes. Columns 6 and 7 give equatorial and galactic coordinates, respectively. Finally, Cols. 8 and 9 give parallaxes with errors and distances, respectively. These two latter columns are taken from the recent compilation given by van Leeuwen (2007, 2008). Parallax errors are typically less than 1 mas, although there are few stars with errors larger than 2 mas; those stars are either spectroscopic binaries or are listed in the Catalogue of the Components of Double and Multiple Stars (CCDM) (Dommanget & Nys 2002) as orbit/astrometric binaries. There are 10 stars in Table 1 with distances between 20 and 25 pc. Those are the previously mentioned stars with known exoplanets (HIP 3497, HIP 25110 and HIP 109378), and with identified *Spitzer* debris discs (HIP 14954, HIP 51502, HIP 72603, HIP 73100, HIP 103389 and HIP 114948). In addition, the distance to HIP 36439 is 20.24 pc (π = 49.41 mas) after the revised HIPPARCOS catalogue (van Leeuwen 2008) but 19.90 pc (π = 50.25 mas) after the original one (ESA 1997). We also note that the distance to HIP 73100 is 25.11 pc (π = 39.83 mas) after van Leeuwen (2008), but 24.84 pc (π = 40.25 mas) after ESA (1997).

Tables 3 (a, b, c and d) give the optical, near-IR, AKARI, WISE, IRAS and *Spitzer* MIPS magnitudes and fluxes of the DUNES stars, while Table 4 gives various stellar parameters. Appendix B gives some details on how the stellar properties were collected. Figure 2 shows the ($B - V$, M_v) and ($V - K$, M_v) colour–magnitude diagrams of the sources where one can see how they spread across the stellar main-sequence. The K-type star located within the G-type locus is HIP 2941. This is likely a misclassification of HIPPARCOS; in fact, the range of spectral types in Skiff (2009) indicates an earlier type, G5V–G9V. This is also supported by the high effective temperature, $T_{\rm eff} \sim 5500$ K (Table 4), too high for a K1 star. The main stellar parameters ($T_{\rm eff}$, $\log g$ and [Fe/H]) were used to compute a set of synthetic spectra from the PHOENIX code for GAIA (Brott & Hauschildt 2005), which were later normalized to the observed SEDs of
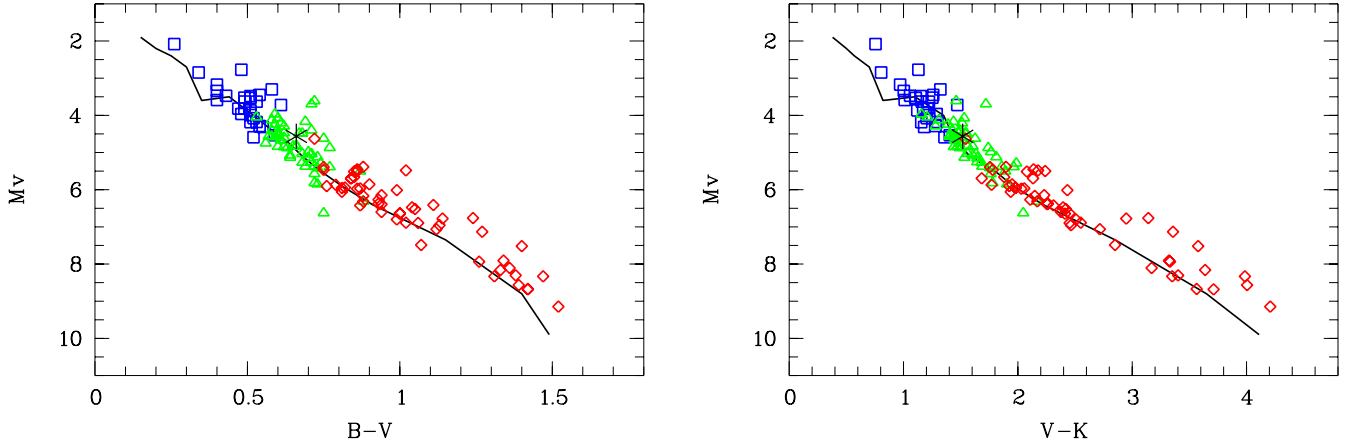
---

[3] http://sdc.cab.inta-csic.es/dunes/

Fig. 2. Colour-absolute magnitude diagrams of the DUNES sources. Spectral types as in Table 1 are distinguished by symbols: blue squares (F-type), green triangles (G-type) and red diamonds (K-type). The solid line in both diagrams represents the main-sequence while the star symbol indicates the position of the Sun (Cox 2000).

Table 5. Summary of all DUNES PACS observations, including the 100/160 and 70/160 channel combinations.

HIP	PACS	Scan	X-Scan	On-source time [s]
171	100/160	1342212800	1342212801	900
544	100/160	1342213512	1342213513	1440
910	100/160	1342199875	1342199876	360
2941	100/160	1342212844	1342212845	540
3093	70/160	1342213242	1342213243	180

Notes. The Obs Ids of both cross-scans (Cols. 3 and 4) and on-source integration time are given. Only the first 5 lines of the table are presented here; the full version is available at the CDS.

the stars in order to estimate the photospheric fluxes at the *Herschel* bands. The whole procedure is described in detail in Appendix C.

4. *Herschel* observations and data reduction

4.1. PACS observations

PACS scan map observations of all 133 DUNES targets (comprising 130 individual fields, due to close binaries allowing doubling up of sources in the cases of HIP 71382/4, HIP 71681/3 and HIP 104214/7) were taken with the 100/160 channel combination. Additional 70/160 observations were carried out for 47 stars, some of them with a *Spitzer* MIPS 70 μm excess. Following the recommended parameters laid out in the scan map release note[4] each scan map consisted of 10 legs of 3′ length, with a 4″ separation between legs, scanning at the medium slew speed (20″ per second). Each target was observed at two array orientation angles (70° and 110°) to improve noise suppression and to assist in the removal of low frequency (1/f) noise, instrumental artifacts and glitches from the images. A summary of the PACS observations can be found in Table 5 where the PACS bands, the observation identification number of each scan, and the on-source integration time are given.

---

[4] See: PICC-ME-TN-036 for details.

Table 6. Summary of DUNES SPIRE observations.

HIP	Obs Id	Time [s]
544	1342213493	74
7978	1342195666	185
13402	1342213481	74
15371	1342198448	185
17439	1342214553	74
22263	1342203629	185
32480	1342204066	185
40843	1342219959	74
51502	1342214703	74
72603	1342213475	74
83389	1342198192	185
84862	1342203593	185
85235	1342213451	74
85295	1342203588	185
92043	1342204948	185
101997	1342206205	185
105312	1342209303	185
106696	1342206206	185
107649	1342209300	185
108870	1342206207	185

Notes. Obs Ids and observing time are given.

4.2. SPIRE observations

SPIRE small map observations were taken of 20 DUNES targets selected because they were known as excess stars or as follow-up to the results of the PACS observations. Each SPIRE observation was composed of either two or five repeats (equivalent on-source time of either 74 or 185 s) of the small scan map mode[5], producing a fully sampled map covering a region 4′ around the target. A summary of the SPIRE observations, observation identification and on-source integration time, is presented in Table 6.

4.3. Data reduction

The PACS and SPIRE observations were reduced using the *Herschel* Interactive Processing Environment, HIPE (Ott 2010), user release version 7.2, PACS calibration version 32 and SPIRE

---

[5] See: http://herschel.esac.esa.int/Docs/SPIRE/html/spire_om.pdf for details.

calibration version 8.1. The individual PACS scans were processed with a high pass filter to remove background structure, using high pass filter radii of 15 frames at 70 μm, 20 frames at 100 μm and 25 frames at 160 μm, suppressing structure larger than 62″, 82″ and 102″ in the final images, respectively. For the filtering process, regions of the map where the pixel brightness exceeded a threshold defined as twice the standard deviation of the non-zero flux elements in the map were masked from inclusion in the high pass filter calculation. Deglitching was carried out using the second level spatial deglitching task, following issues with the clipping of the cores of bright sources using the MMT deglitching method. The two individual PACS scans were mosaicked to reduce sky noise and suppress $1/f$ stripping effects from the scanning. Final image scales were 1″ per pixel at 70 and 100 μm and 2″ per pixel at 160 μm compared to native instrument pixel sizes of 3.″2 and 6.″4. For the SPIRE observations, the small maps were created using the standard pipeline routine in HIPE, using the naive mapper option. Image scales of 6″, 10″ and 14″ per pixel were used at 250 μm, 350 μm and 500 μm, respectively.

5. Noise analysis of the DUNES PACS images

The DUNES sample is mostly composed of faint targets in the far-IR. Their fluxes are negligible compared to the telescope thermal emission, which is the main contributor in the form of a large background. Confusion noise is also a concern for some very deep observations, particularly for the 160 μm band. The optimum S/N ratio is affected by the choice of the aperture to estimate the source flux and the background. Poisson statistics describe the energy collected from both noise sources: thermal emission and confusion.

The map noise properties can be studied using two different metrics: i) $\sigma_{\rm pix}$ is the dispersion of the background flux measured on regions sufficiently large to avoid small number statistics, and sufficiently small to avoid the effects of large scale sky inhomogeneities, e.g. cirrus. $\sigma_{\rm pix}$ is best estimated taking the median value of several such areas in the image. ii) $\sigma_{\rm sky}$ is the standard deviation of the flux collected by several apertures placed in clear areas in the central portion of the image.

In an ideal scenario with purely random high Poisson noise, both parameters would be related by:

$$\sigma_{\rm sky} = \sigma_{\rm pix}\alpha_{\rm corr}\sqrt{N_{\rm pix}^{\rm circ}} \qquad (1)$$

where $N_{\rm pix}^{\rm circ}$ is the total number of pixels in a circular aperture and $\alpha_{\rm corr}$ is the noise correlation factor. However, the real far-IR sky is far from homogeneous, specially for wavelengths around 160 μm. In addition, the reduction procedure is not perfect and some residual artificial structure appears superimposed. This "corrugated" noise usually makes $\sigma_{\rm sky}$ be larger than the expected value from Eq. (1).

Noise correlation is a feature of PACS scan maps that appears because the signal in a given output pixel partially depends on the values recorded in the neighborhood. Correlations appear due to three main reasons. First, the scan procedure entangles the output pixel counts via the signal recorded by the discrete bolometers at a given time. Second, the output maps have pixels much smaller than the real pixel size of the bolometers, which is done with the aim of providing better spatial resolution. Third, the $1/f$ noise introduced by small instabilities in the array temperature and electronics.

5.1. Signal to noise ratio and optimal aperture

Aperture photometry estimates the flux of a source integrating in a circle centered on it and containing a significant fraction of the flux. The flux is given by:

$$\text{Signal} = F_\star \text{EEF}(r) \qquad (2)$$

where $F_\star$ is the flux of the point source in the circle with radius r, and EEF(r) is the enclosed energy fraction in the circular aperture. The radius is chosen to maximize the signal to noise ratio. The noise has two main contributions. The uncertainty in the flux inside the aperture, Noise$_\star$, and the uncertainty in the background, Noise$_{\rm back}$. There are two ways to estimate the noise, based on the metrics $\sigma_{\rm pix}$ and $\sigma_{\rm sky}$.

In terms of $\sigma_{\rm pix}$, the aperture noise is given by:

$$\text{Noise}_\star = \sigma_{\rm pix}\alpha_{\rm corr}\sqrt{N_{\rm pix}^{\rm circ}} = \sigma_{\rm pix}\alpha_{\rm corr}\sqrt{\pi}r_{\rm pix}. \qquad (3)$$

The background flux is typically determined using an annulus of inner $r_{\rm i}$ and $r_{\rm o}$ outer radii (pixel units). The flux coming from the point source at the location of the annulus due to the large extension of the point spread function (PSF) is assumed negligible compared to the noise, because the DUNES sources are typically faint. The background noise contribution can be estimated as:

$$\text{Noise}_{\rm back} = \sigma_{\rm pix}\alpha_{\rm corr}N_{\rm pix}^{\rm circ}\Big/\sqrt{N_{\rm pix}^{\rm annulus}} =$$
$$\sigma_{\rm pix}\alpha_{\rm corr}\sqrt{\pi}r_{\rm pix}^2\Big/\sqrt{r_{\rm o}^2 - r_{\rm i}^2}. \qquad (4)$$

The total noise is the quadratic sum of both the aperture and background contributions:

$$\text{Noise} = \sqrt{\text{Noise}_\star^2 + \text{Noise}_{\rm back}^2}. \qquad (5)$$

Alternatively, in terms of $\sigma_{\rm sky}$ the sky background and the associated uncertainty can be estimated measuring the total flux in $n_{\rm sky}$ apertures with the same size used for the source. The apertures are located in clean fields, in order to avoid biasing the statistics, and as close as possible to the source, in order to get uniform exposure times. In this case, the noise is given by:

$$\text{Noise} = \sigma_{\rm sky}\sqrt{1 + \frac{1}{n_{\rm sky}}}. \qquad (6)$$

The $1/n_{\rm sky}$ factor comes from the finite number of apertures used and quickly goes to zero. This approach has the advantage that no correlated noise factor is required for sufficiently large apertures. However, it provides a conservative estimate if the background is variable, due to sky inhomogeneities or $1/f$ noise filtering residuals, as it is the case for the DUNES observations.

In order to validate the consistency of both noise estimation procedures we have carried out several tests using both survey reduced images and synthetic noise frames. The theoretical relationship between $\sigma_{\rm sky}$ and $\sigma_{\rm pix}$ in Eq. (1) has been tested for small to moderately large box sizes, which is a way to verify the error propagation scheme under large Poisson noise conditions. For the synthetic noise frames, we have built an image of 200$\times$200 pixels with an arbitrarily large sky level of 10 000 photons and Gaussian noise of 100 photons, since the Poisson distribution can be well approximated by a Gaussian for high fluxes. This image simulates the noise introduced by the telescope emission, which is the dominant factor for DUNES – faint sources and broad band photometry. Multiple regions (25+) have been

Table 7. Gaussian noise propagation in the absence of noise correlation.

Box size (pix)	σ_{pix}	σ_{sky}	$\sigma_{\mathrm{pix}} \sqrt{N_{\mathrm{pix}}}$
7	100	610	698
15	101	1310	1520
22	100	2290	2200

Notes. The RMS dispersion of the sky flux σ_{sky} in different windows is consistent with propagating the single pixel uncertainty σ_{pix} according to the window size in pixels N_{pix}.

selected in the image with square box sizes of 7, 15 and 22 pixels per side. σ_{pix} and σ_{sky} have been estimated for these boxes, and the latter values have been compared to $\sigma_{\mathrm{pix}} \sqrt{N_{\mathrm{pix}}}$ (Table 7). The differences are below 15%, consistent with Poisson propagation noise. It has thus been verified that noise propagation works well for images not affected by correlated noise. In addition, small boxes can be used to provide reliable estimates.

Further, a comparison of both methods by the HSC team (Altieri, priv. comm.) showed that the multiple apertures σ_{sky} method provides in general larger uncertainties than the error propagation of the σ_{pix} metrics. The values are typically consistent and smaller than a factor 2. The selection of one of them is subjective. Given that the aim of DUNES is the detection of very faint excesses, we have followed the conservative approach of taking the largest noise value for each individual DUNES source to assess the presence of an infrared excess.

Finally, when the sky value has been determined with high precision (using many apertures to improve the statistics), the signal to noise ratio can be estimated as:

$$\mathrm{SNR}(r_{\mathrm{pix}}) = \frac{F_{\star} \mathrm{EEF}(r_{\mathrm{pix}})}{\mathrm{Noise}}. \tag{7}$$

This equation shows that there is an optimum extraction radius providing the highest SNR possible. If it is too small, little signal will be collected, while if it is too large, the noise introduced by the aperture is considerable. Optimum values estimated by the *Herschel* team[6] are 4″, 5″ and 7″–8″ for 70, 100 and 160 μm, respectively. We have carried out the same exercise using a number of DUNES clean fields and the σ_{pix} metrics (σ_{sky} is comparatively more affected by sky inhomogeneities) and found essentially the same results.

5.2. Correlated noise

As pointed out before, the PACS scan map observations intrinsically suffer from correlated noise. Theoretical correlated noise factors α_{corr} were derived by Fruchter & Hook (2002) for the Drizzle algorithm, which combines multiple undersampled images (in terms of the Nyquist criterion). They showed that the correlated noise depends on the ratio r between the linear pixel fraction (the ratio between the drop and the natural pixel box sizes) and the linear output pixel scale factor (the ratio between the output and the natural pixel box sizes). This procedure, used by default in the *Herschel* PACS reduction pipeline, produces output images with typical smaller output pixel sizes, better spatial resolution than individual frames, but significant correlated noise.

The PACS calibration team has made extensive tests on the correlated noise measuring the noise properties of fields

---

[6] Technical Note PICC-ME-TN-037 in http://herschel.esac.esa.int

surrounding bright stars (see the mentioned technical note PICC-ME-TN-037) and have estimated α_{corr} as a function of the output pixel size. The value for output pixel sizes of 1″ (the size of our 100 μm reduced images) is $\alpha_{\mathrm{corr}} = 2.322$, while for 2″ (160 μm images) $\alpha_{\mathrm{corr}} = 2.656$. However, these estimates are too optimistic because no correlated noise is assumed for output pixels with a size equal to the natural ones.

We have analysed the effect of the correlated noise on images with natural pixel sizes as it has a clear effect on the α_{corr} factor we have to apply for our reduced images. The approach we have made is the following.

As a first step, we have tried to validate the PICC-ME-TN-037 predictions evaluating the noise properties of the PACS images of the DUNES stars HIP 103389, HIP 107350 and HIP 114948. Reduced observations with both small (1″/pix, 70 and 100 μm and 2″/pix, 160 μm) and natural (3.2″/pix, 70 and 100 μm and 6.4″/pix, 160 μm) pixel sizes have been considered. Square box sizes of 22″ and 44″ have been used for 100 and 160 μm, respectively. These values, larger than the optimal aperture sizes, were used to prevent small number statistics for the natural pixel size frames. Table 8 summarises the results, from which several conclusions can be drawn. i) The correlated noise effect can clearly be noticed comparing the $\sigma_{\mathrm{pix}} \sqrt{N_{\mathrm{pix}}}$ values, which are much smaller for the small size output pixels. This means that there is indeed significant correlated noise in the finer sampled output frames. ii) Similar statistical flux uncertainties $\Delta F_{\star} = \alpha_{\mathrm{corr}} \sigma_{\mathrm{pix}} \sqrt{N_{\mathrm{pix}}}$ are obtained for aperture photometry if the correlation factors in PICC-ME-TN-037 are used. The agreement is better for the blue detectors. This demonstrates that the PICC-ME-TN-037 α_{corr} formulae provide good estimates of the differential increase in correlated noise between natural size and smaller output pixels. However, the amount of correlated noise for natural size output pixels is unknown. iii) The sky value, when averaged over a large area, is not affected by correlated noise. It can, nevertheless, be affected by large scale sky inhomogeneities due to residual $1/f$ noise or confusion (partially resolved background sources).

As a second step, the full correlated noise factors for small and natural pixel sizes have been estimated. Additional tests were carried out reducing the HIP 544 and HIP 99240 images with different output pixel sizes. These objects are in fields particularly clean of additional sources, which is critical to really estimate correlated noise factors and not confusion noise. The output pixel sizes range between the standard 1″ and 2″ for 100 and 160 μm, and twice the natural pixel size, respectively. The pixel fraction was always set to the default value of 1.0. For each image and pixel size, σ_{pix} was estimated on sky constant size boxes of $\approx$25″ and 50″ widths for the 100 and 160 μm channels, respectively. The results are presented in Table 9. It shows the median value σ_{pix} of each frame estimated as the median of several measurements ($\sim$6–8) in boxes placed next to the central object, to minimise sky coverage border effects. Correlated noise factors in the table have been computed assuming no correlated noise for the images with output pixels twice the natural size ($r = 0.50$). This assumption is not strictly correct. However, larger output pixel sizes could not be studied because the box sizes required would have been too large compared to the high density coverage portion in the DUNES small scan maps. In addition, very large output pixel sizes make rejection of background sources increasingly difficult. We believe the small amount of correlated noise not considered for the very large pixels compensates with the additional background noise included in the box averages.

Table 8. Image noise properties for small and natural output pixel sizes.

Unit: Jy Image	Small pix $\sigma_{\rm sky}$	$\sigma_{\rm pix}\sqrt{N_{\rm pix}}$	Natural pix $\sigma_{\rm sky}$	$\sigma_{\rm pix}\sqrt{N_{\rm pix}}$	Error ratio $\Delta F_\star^{\rm natural}/\Delta F_\star^{\rm small}$
HIP 103389 70	3.32e-03	1.02e-03	3.84e-03	2.31e-03	1.01
HIP 103389 100	2.02e-03	3.62e-04	1.50e-03	8.64e-04	1.06
HIP 107350 100	1.34e-03	3.42e-04	1.46e-03	8.73e-04	1.14
HIP 114948 100	1.23e-03	3.48e-04	1.01e-03	8.18e-04	1.05
HIP 103389 160 a	1.08e-02	2.48e-03	6.18e-03	6.42e-03	1.23
HIP 103389 160 b	3.15e-03	1.17e-03	3.32e-03	2.94e-03	1.19
HIP 107350 160	5.76e-03	1.07e-03	4.40e-03	2.68e-03	1.19
HIP 114948 160	4.11e-03	1.18e-03	3.56e-03	3.11e-03	1.25

Notes. $\sigma_{\rm sky}$ and $\sigma_{\rm pix}$ have been estimated for several fields using clean square areas of 22″ and 44″ sizes at 100 and 160 μm, respectively. The number after the stellar HIPPARCOS catalogue number is the wavelength: 70, 100 and 160 μm. Two different 160 μm images were available for HIP 103389. The correlated noise is clearly revealed by $\sigma_{\rm sky}$ being always larger than $\sigma_{\rm pix}\sqrt{N_{\rm pix}}$ for the small output pixels. The correlated factors included in PIC-ME-TN-037 have been used to compute the error ratios $\Delta F_\star^{\rm natural}/\Delta F_\star^{\rm small} = \alpha_{\rm corr}^{\rm natural}\sigma_{\rm pix}^{\rm natural}\sqrt{N_{\rm pix}^{\rm natural}}/\alpha_{\rm corr}^{\rm small}\sigma_{\rm pix}^{\rm small}\sqrt{N_{\rm pix}^{\rm small}}$. The ratios are always close to 1.0, which means that the factors in PIC-ME-TN-037 account for the difference in correlated noise between the natural and standard output pixel sizes. See text and Table 9 for more details on the correlated noise factor for natural output pixel sizes.

Table 9. Clean field correlated noise estimation.

r	HIP 544 100 μm $\sigma_{\rm pix}$ (Jy)	$\alpha_{\rm corr}$	HIP 544 160 μm $\sigma_{\rm pix}$ (Jy)	$\alpha_{\rm corr}$	HIP 99240 100 μm $\sigma_{\rm pix}$ (Jy)	$\alpha_{\rm corr}$	HIP 99240 160 μm $\sigma_{\rm pix}$ (Jy)	$\alpha_{\rm corr}$
3.20	1.91e-05	3.88	5.91e-05	3.61	4.69e-05	3.36	1.14e-04	3.73
1.47	7.79e-05	2.07	2.50e-04	1.85	1.89e-04	1.81	5.05e-04	1.83
1.00	1.56e-04	1.53	5.13e-04	1.33	3.60e-04	1.40	1.05e-03	1.30
0.67	3.09e-04	1.15	8.84e-04	1.16	6.87e-04	1.10	1.97e-03	1.04
0.50	4.75e-04	1.00	1.36e-03	1.00	1.01e-03	1.00	2.73e-03	1.00

Notes. The correlated noise factors $\alpha_{\rm corr}$ are estimated as the ratio between the $\sigma_{\rm pix}$ value obtained for the largest output image pixel size (twice the natural pixel size) and the size of interest. No correlation noise is assumed for the largest output image pixel size. The box size is approximately constant for all output pixel sizes: ~25″, 50″ for 100 and 160 μm, respectively.

The correlated noise factors in Table 9 are roughly consistent with the predictions by Fruchter & Hook (2002). In particular, the values obtained for the fine pixel maps (1″/pix and 2″/pix for 100 and 160 μm) bracket the theoretical expectations. Taking into account all the tests carried out, the correlated noise factor that has been used for the analysis of the whole DUNES sample and all wavelengths is: $\alpha_{\rm corr,DUNES} = 3.7$. It is the same for all 70, 100 and 160 μm because the ratio between natural to standard output pixel sizes is always 3.2.

6. Results

6.1. PACS

6.1.1. PACS photometry

PACS photometry of the sources identified as the far-IR counterparts of the optical stars was carried out using two different methods. The first method consisted in estimating PACS fluxes primarily using circular aperture photometry with the optimal radii 4″, 5″, and 8″ at 70 μm, 100 μm and 160 μm, respectively. For extended sources, the beam radius was chosen large enough to cover the whole extended emission. The corresponding beam aperture correction as given in the technical note PICC-ME-TN-037 was taken into account. The reference background region was usually taken in a ring of width 10″ at a separation of 10″ from the circular aperture size. Nonetheless we took special care to choose the reference sky region for those objects where the "default" sky was or could be contaminated

by background objects. In addition, we also carried out complete curve of growth measurements with increasing apertures and the corresponding skies. Sky noise for each PACS band was calculated from the rms pixel variance of ten sky apertures of the same size as the source aperture and randomly distributed across the uniformly covered part of the image (pixel sky noise from the curves of growth are essentially identical). Final error estimates take into account the correlated noise factor estimated by us (see previous section) and aperture correction factors. Figure 3 (top) shows a plot of the mean sky noise value at 100 μm obtained for all images with the same on-source integration time versus the on-source integration time. Error bars are the rms standard deviation of the sky noise values measured in the images taken with the same on-source time; we note that the number of images is not the same for each integration time, so that those error bars are only indicative of the noise behaviour. The plot also shows a curve of the noise assuming that the S/N ratio varies with the square root of the time. The curve is normalized to the mean sky noise value of the images with the shortest integration time, 360 s, showing that the PACS 100 μm images are essentially background limited. Figure 3 (bottom) is the same plot at 160 μm; the curve is also normalized to the shortest on-source integration time. The 160 μm noise behaviour is flatter than the $S/N \propto t^{1/2}$ curve, suggesting that it is influenced by structured background diffuse emission, and that is confusion limited for integration times longer than around 900 s. With the second method we carried out photometry using rectangular boxes with areas equivalent to the default circular apertures; in this case, we chose box sizes large enough to cover the whole
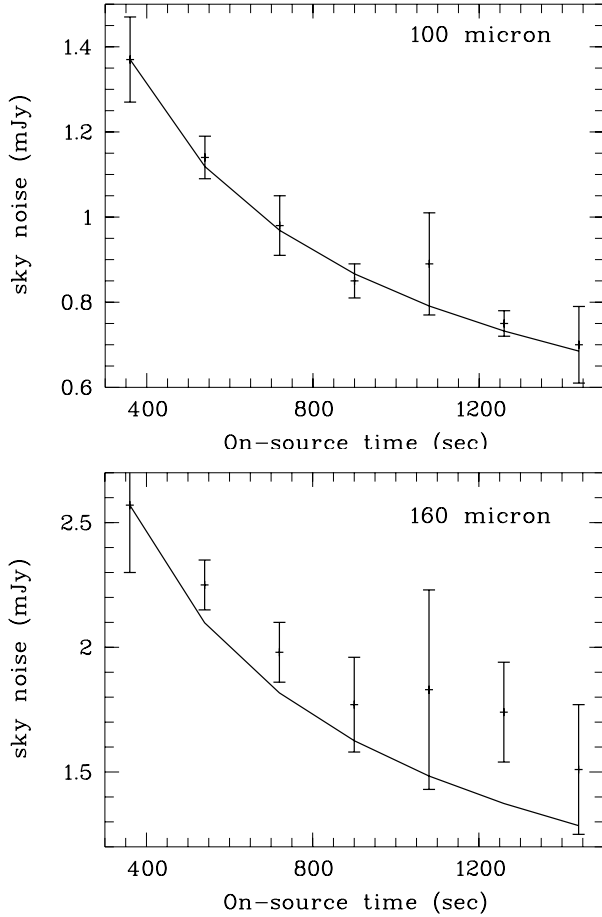
Fig. 3. *Top*: mean value of the sky noise estimates at 100 μm versus on-source integration time. Error bars are the rms standard deviation of the sky noise in the images taken with the same on-source observing time. The solid curve represents the noise behaviour assuming that the S/N ratio varies as the square root of the time, normalized by the mean value of the images with an on-source exposure time of 360 s. *Bottom*: the same for the 160 μm images.

emission for extended sources. Sky level and sky rms noise from this method were estimated from measurements in ten fields, selected as clean as possible by the eye, of the same size as the photometric source boxes. Photometric values and errors take into account beam correction factors. The estimated fluxes from both methods, circular and rectangular aperture photometry, agree within the errors. PSF photometry of point sources using the DAOPHOT software package was also carried out for those cases where a nearby object is present and prevents us from using any of the two methods above. The fluxes using aperture photometry and DAOPHOT are consistent within the uncertainties for point sources in non-crowded fields. However, the errors provided by DAOPHOT are too optimistic by a typical factor of an order of magnitude. This is a consequence of correlated noise, which cannot easily be handled by DAOPHOT. Using $\alpha_{corr}\,\sigma_{pix}$ as the flux uncertainty for each pixel does not solve the problem. The errors for DAOPHOT photometry have thus been estimated using the formulae derived for standard DUNES aperture photometry. The noise introduced by source crowding is considered negligible as compared to the other major contributors: thermal noise background, stellar flux determination and PACS absolute photometric calibration uncertainties. The absolute uncertainties in this version of HIPE are 2.64% (70 μm), 2.75% (100 μm) and 4.15% (160 μm), as indicated in the cited technical note.

Table 10. Optical and PACS 100 μm equatorial positions (J2000) of the DUNES stars together with the positional offset between both nominal positions.

HIP	ICRS(2000)	PACS100	Offset (arcsec)
171	00 02 10.16 +27 04 56.1	00 02 10.57 +27 04 56.0	5.5
544	00 06 36.78 +29 01 17.4	00 06 36.79 +29 01 15.8	1.6
910	00 11 15.86 −15 28 04.7	00 11 15.88 −15 28 03.4	1.3
2941	00 37 20.70 −24 46 02.2	00 37 20.54 −24 46 03.9	2.8
3093	00 39 21.81 +21 15 01.7	00 39 21.84 +21 14 58.9	2.8

Notes. Only the first 5 objects of the sample are presented here; the full version of the table is available at the CDS.
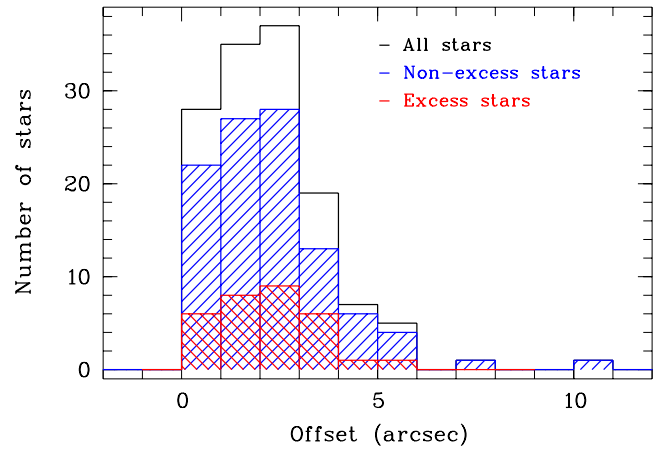

Fig. 4. Histograms of the offset position between the optical and the PACS 100 μm coordinates. Histograms are shown for the whole DUNES sample of stars, the non-excess stars and excess star candidates. The spurious sources (see Sect. 7.1) are included as non-excess stars in this figure.

6.1.2. Pointing: excess/non-excess sources

PACS at 100 and 160 μm are very sensitive to background objects, usually red galaxies and, therefore, there is a non-negligible chance of contamination (Sect. 7.2.1) Thus, it is necessary to check the agreement between the optical position of the stars and the one of the objects identified as their *Herschel* counterparts – as well as in the cases of non-excess sources the agreement between the measured PACS fluxes and the predicted photospheric levels (Sect. 7.1). Table 10 gives the J2000.0 optical equatorial coordinates and the PACS positions at 100 μm, corrected from the proper motions of the stars as given by van Leeuwen (2008). Figure 4 shows histograms of the positional offset between the optical and PACS 100 μm positions for all the stars, as well as separately for the non-excess (including here the spurious sources, see below) and excess sources. In all three stellar samples ~65% of the stars have offsets less than 2".4, which is the expected *Herschel* pointing accuracy[7], while there are 5 non-excess stars and only one excess star with positional offsets >2σ. In this respect we note that based on a grid of known 24 μm sources, Berta et al. (2010) found absolute astrometric offsets in the GOODS-N field as high as 5″.

The non-excess sources with offsets >2σ are: HIP 28442, HIP 34065, HIP 54646, HIP 57939 and HIP 71681 (α CenB – HIP 71683 is α CenA and has an offset of 4".2). These

---

Table 11. SPIRE fluxes (Fλ) with 1σ errors, together with the photospheric predictions (Sλ).

HIP	F250 (mJy)	S250 (mJy)	χ250	F350 (mJy)	S350 (mJy)	χ350	F500 (mJy)	S500 (mJy)	χ500
544	<22.5	1.20 ± 0.03		<24.3	0.61 ± 0.02		<27.6	0.30 ± 0.01	
7978	312.30 ± 25.60	1.37 ± 0.08	12.15	179.90 ± 14.60	0.70 ± 0.04	12.27	78.40 ± 9.80	0.34 ± 0.02	7.97
13402	<23.1	1.63 ± 0.03		<23.1	0.83 ± 0.02		<28.2	0.41 ± 0.01	
15371	59.72 ± 6.70	2.03 ± 0.03	8.61	24.68 ± 6.89	1.04 ± 0.02	3.43	20.29 ± 7.66	0.51 ± 0.01	2.58
17439	53.00 ± 10.40	0.68 ± 0.01	5.03	32.20 ± 8.90	0.35 ± 0.01	3.58	<21.6	0.17 ± 0.01	
22263	23.21 ± 6.81	1.66 ± 0.03	3.16	14.14 ± 6.87	0.85 ± 0.02	1.93	<28.8	0.42 ± 0.01	
32480	90.00 ± 15.00	1.75 ± 0.02	5.88	25.00 ± 8.00	0.89 ± 0.01	3.01	<24.0	0.44 ± 0.01	
40843	<24.0	1.77 ± 0.01		<23.7	0.90 ± 0.01		<26.4	0.44 ± 0.01	
51502	49.65 ± 8.29	1.30 ± 0.02	5.83	41.01 ± 8.15	0.66 ± 0.01	4.95	23.10 ± 9.41	0.33 ± 0.01	2.42
72603	<24.0	1.43 ± 0.01		<24.3	0.73 ± 0.01		<30.9	0.36 ± 0.01	
83389	<20.1	0.64 ± 0.01		<21.0	0.33 ± 0.01		<24.0	0.16 ± 0.01	
84862	<20.1	1.95 ± 0.02		<21.0	0.99 ± 0.01		<24.3	0.49 ± 0.01	
85235	<22.2	1.00 ± 0.02		<23.1	0.51 ± 0.01		<29.4	0.25 ± 0.01	
85295	<19.8	1.66 ± 0.04		<21.0	0.85 ± 0.02		<24.0	0.42 ± 0.01	
92043	12.12 ± 6.57	3.85 ± 0.05	1.26	<21.9	1.96 ± 0.03		<24.3	0.96 ± 0.01	
101997	<19.5	0.91 ± 0.02		<21.0	0.46 ± 0.01		<24.6	0.23 ± 0.01	
105312	<19.8	0.93 ± 0.05		<20.7	0.47 ± 0.03		<24.0	0.23 ± 0.01	
106696	<19.5	0.65 ± 0.01		<20.7	0.33 ± 0.01		<24.9	0.16 ± 0.01	
107649	113.00 ± 18.00	1.44 ± 0.02	6.20	44.30 ± 9.00	0.73 ± 0.01	4.84	25.90 ± 8.00	0.36 ± 0.01	3.19
108870	<19.8	9.86 ± 0.23		<21.0	5.03 ± 0.12		<23.4	2.47 ± 0.06	

Notes. The significance at each band is given. Figures without errors in the SPIRE columns give 3σ upper limits for the corresponding stars.

non-excess sources, excluding α Cen, are faint with no or dubious (the case of HIP 34065) 160 μm detection, but their estimated 100 μm fluxes agree well with the photospheric predictions, $|F_{PACS100} - F_{star}| < 1.6$ mJy. HIP 57939 has an extremely high proper motion; the rest are multiple stars. HIP 28442, which shows a very large offset, the largest one, is an outlier. However, it has a very large parallax error (21 mas) and is a member of a quadruple star, CCDM J06003-3103ABC; its optical and 2MASS coordinates differ around 6″ – in fact, the offset between the PACS 100 μm and 2MASS coordinates is only of ~4″. Further, the accuracy of its proper motion is somehow dubious. After the proper motion values as given in the LHS catalogue (Luyten 1979) the offset between the optical and *Herschel* positions would just be ≈4″, but the revised version of that catalogue (Bakos et al. 2002) presents proper motions similar to those of HIPPARCOS. Thus, the real offset remains unsolved. In the case of α Cen the offset values in Table 10 do not take into account its orbital motion. Correcting from that orbital motion we find an offset for α Cen A relative to the pointed position of 1″7 at 100 μm, i.e., well below the 1σ pointing accuracy (Wiegert et al., in prep.). We do not have orbital motion information for the rest of the multiple sources. Finally, the offset between the nominal optical position and the 100 μm peak of the star HIP 40843 (Fig. D.1) is 7″1, but this result most likely reflects a case of coincidental alignment (see Sect. 7.2.1 and Appendix D).

The excess-source with offset >2σ is HIP 171. Again this object is a binary with a separation between components of 0″83, the component B being a binary itself (Bach et al. 2009). We do not have information on the orbital motion so that the PACS 100 μm position cannot be corrected, but its 100 μm flux is very well in agreement with the photospheric prediction of the multiple system, $|F_{PACS100} - F_{star}| < 1.0$ mJy (Sect. 7.2).

6.2. SPIRE

The method of flux measurement in the SPIRE maps was dependent on the expected source brightness and extent (compared

to the instrument PSF) in each band, following the recommendations of the SPIRE data reduction guide[8] (see SPIRE DRG Fig. 5.57, Sect. 5.7). In the case of extended sources (HIP 7978, HIP 32480 and HIP 107649), flux measurement was made via aperture photometry with aperture radii large enough to cover the source and a sky annulus of 60″–90″. In the case of point sources brighter than 30 mJy (HIP 544, HIP 13402, HIP 17439 and HIP 22263), the timeline fitter task was used to estimate the photometry using aperture radii of 22″ at 250 μm, 30″ at 350 μm and 42″ at 500 μm with a background annulus of 60″–90″ for all three bands. Finally, in the case of sources fainter than 30 mJy or non-detections, the SUSSEXtractor tool was used to estimate the flux or 3-σ upper limits from the sky background and rms, as appropriate. A summary of the SPIRE photometry is presented in Table 11 and the flux values are plotted in Fig. E.1.

7. Analysis

7.1. Non-excess sources

We consider that a star has an infrared excess at any PACS wavelength when the significance, $\chi\lambda = (PACS\lambda - S\lambda)/\sigma$, is larger than 3, where PACSλ is the measured flux, Sλ is the predicted photospheric flux and σ is the total error. The predicted fluxes are based on a Rayleigh-Jeans extrapolation from the 40 μm fluxes estimated from the PHOENIX/GAIA LTE atmospheric models (see Appendix C). The sources for which no clear excesses are detected at any of the *Herschel* PACS bands are listed in Table 12, where the PACS fluxes, photospheric predictions, and significance of the detections at each PACS band are given. Figures without errors in the PACS160 column give 3σ upper limits. Errors of the PACS fluxes are the quadratic sum of the photometric errors and the absolute calibration uncertainties; for the photometric errors, we have taken the conservative approach of choosing the largest error values estimated either from the circular (σ_{pix} metric) or from the rectangular aperture

---

[8] http://herschel.esac.esa.int/hcss-doc-9.0

Table 12. PACS fluxes with 1σ errors of non-excess sources, together with the photospheric predictions ($S\lambda$).

HIP	SpT	PACS70	S70	χ_{70}	PACS100	S100	χ_{100}	PACS160	S160	χ_{160}	$L_d/L_\star$	MIPS70
910	F5V		29.51 ± 0.19		17.66 ± 1.38	14.46 ± 0.09	2.32	<7.5	5.61 ± 0.04		8.9e-07	37.50 ± 4.48
2941	K1V+...		24.09 ± 0.43		11.20 ± 1.82	11.80 ± 0.21	-0.33	<5.7	4.61 ± 0.08		2.0e-06	25.80 ± 11.93
3093	K0V	21.93 ± 1.69	22.50 ± 0.34	-0.33	8.21 ± 1.23	11.02 ± 0.17	-2.26	3.76 ± 3.43	4.31 ± 0.07	-0.16	1.7e-06	14.90 ± 5.69
3497	G3V	7.97 ± 0.95	8.72 ± 0.10	-0.78	5.23 ± 1.01	4.27 ± 0.05	0.95	<4.8	1.67 ± 0.02		2.8e-06	5.20 ± 4.41
3821	G0V SB		131.05 ± 2.06		60.80 ± 2.04	64.21 ± 1.01	-1.50	15.75 ± 2.66	25.08 ± 0.39	-3.47	3.3e-07	122.3 ± 10.74

Notes. The significance at each band is given. Figures without errors in the PACS160 column give 3σ upper limits. Figures in the column $L_d/L_\star$ give upper limits of the fractional luminosity of the dust. The last column gives *Spitzer* fluxes at $70\,\mu$m. Units for fluxes and photospheric predictions are mJy. Only the first 5 lines of the table are given here. The full version is available at the CDS.

Table 13. Overall description of the DUNES sample and summary results.

Sample	F stars	G stars	K stars	Total
Solar-type stars observed by DUNES (the DUNES sample)	27	52	54	133
20 pc DUNES subsample	20	50	54	124
Non-excess stars in the whole DUNES sample	16(59%)	37(71%)	42(78%)	95(71%)
Affected by field contamination	2	3	2	7
Excess stars in the whole DUNES sample	9(2)	12(3)	10(5)	31(10)
Excess stars in the 20 pc subsample	4(20%)	11(22%)	10(18.5%)	25(20.2%)
Resolved debris discs	5(4)	6(4)	5(5)	16 (13)

Notes. Percentages in parenthesis refer to the amount of stars in the corresponding spectral types or the whole samples. Single numbers in parenthesis refer to the number of new debris disc stars identified in this survey.
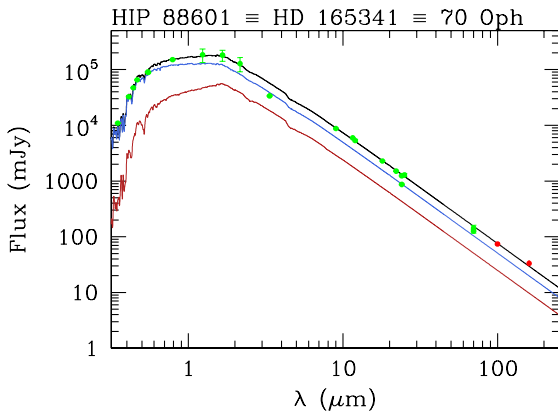

Fig. 5. Spectral energy distribution of the non-excess star HIP 88601. Plotted are optical, near-IR, WISE, and *Spitzer* MIPS (green symbols), as well as the PACS 100 μm and 160 μm (red symbols) fluxes. The photospheric fits of each individual component together with the added contribution of both stars (black) are shown as continuous lines.
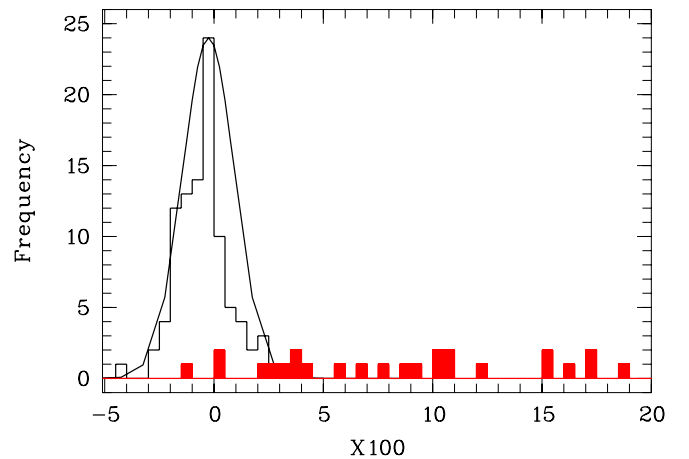

Fig. 6. Histogram of the 100 μm significance for the non-excess (empty histogram) and excess (red filled histogram) sources. The continuous line is a Gaussian with $\sigma = 1.18$, which is the standard deviation of the $\chi 100$ values of non-excess sources. Excess sources with $\chi 100 < 3$ are cold disc candidates (see Sect. 7.2.4).

photometry ($\sigma_{\rm sky}$ metric). Errors of the predicted fluxes are estimated by means of the least reduced χ^2 procedure described in Appendix C. The significance values in Table 12 are estimated taking as the total error the quadratic sum of the PACS and predicted flux errors. *Spitzer* 70 μm MIPS fluxes estimated again for this work are given in the last column of the table. The total number of the non-excess sources are 95 out of 133 ($\sim$71%). The spectral type distribution of this type of objects (see Table 13) is 16 F-type stars ($\sim$59% of the total DUNES F-type stellar sample), 37 G-type stars ($\sim$71% of the G-type) and 42 K-type stars ($\sim$78% of the K-type). As an example of the photospheric fits, Fig. 5 shows the observed SED of the binary star HIP 88601 (V 2391 Oph, 70 Oph AB), where the fit takes into account the contribution of both components (Eggenberger et al. 2008). A histogram of the significance $\chi 100$ of the non-excess sources is shown in Fig. 6. The median value of $\chi 100$ is -0.44, and

the mean value is -0.50 with a standard deviation of 1.18. A Gaussian curve with this σ value is also plotted. If we directly consider the differences between observed and predicted fluxes, we obtain a mean value of the 100 μm flux offset of -0.54 mJy with a standard deviation of 1.40 mJy (α Cen is not included); the median value is -0.60 mJy. We note that the standard deviation of the 100 μm flux offsets is approximately of the same order as the corresponding sky noise value. The difference in flux suggests that we might be detecting a small far-IR deficit between the observed and predicted fluxes This trend, if real, might be reflecting the fact that the extrapolation of the photospheric fits (based on atmospheric models) to the PACS bands does not take into account that in solar-type stars the brightness temperature decreases with the wavelength as the free-free
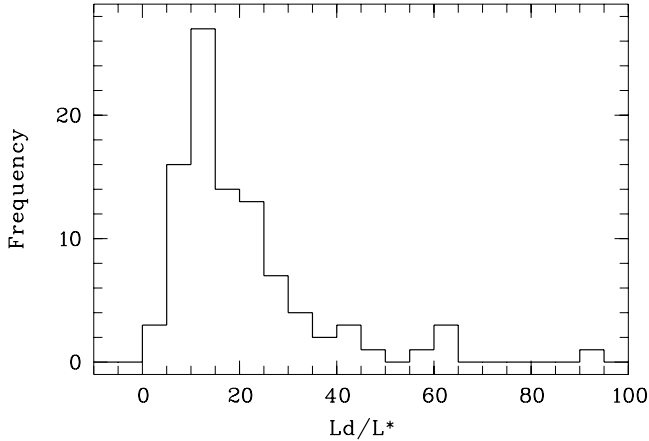
Fig. 7. Histogram of the upper limit of the fractional luminosity of the dust of the non-excess sources. Units: 10^{-7}.

opacity of H^- increases. In the Sun the origin of the far-IR radiation moves to higher regions in the photosphere, the so-called temperature minimum region (Avrett 2003). The apparent weak far-IR deficit we observe in the DUNES sample might at least partly be due to this temperature minimum effect in solar-type stars. In fact, an in-depth analysis of α Cen A using the DUNES *Herschel* data strongly argues for the first measurement of this temperature minimum effect in a star other the Sun (Liseau et al. 2013).

Two stars in Table 12, HIP 40693 and HIP 72603, have *Spitzer* fluxes in excess of the photospheric emission. HIP 40693 (HD 69830) has a well characterized warm debris disc, as shown by the MIPS IRS excess between 8 and 35 μm but no excess at 70 μm (Beichman et al. 2005, 2011); we do not detect any 100 or 160 μm excess with PACS. The *Spitzer* MIPS 70 μm of HIP 72603 (Table 12) suggests the presence of a far-IR excess; however, this is clearly not supported by the *Herschel* data since the observed PACS 70 μm is in very good agreement with the predicted photospheric fluxes, as well the PACS 100 and 160 μm results. The 100 μm aperture photometry flux of HIP 82860 given in Table 12 presents a marginal excess (χ_{100} = 2.7) but it is most likely contaminated by a bright nearby galaxy. PSF photometry gives 13.2 mJy. Both HIP 82860 and the nearby bright background galaxy cannot spatially be resolved at 160 μm. A similar situation is found with HIP 40843 (see Appendix D and Table D.1), whose apparent excesses with *Spitzer* and PACS are most likely due to contamination by a nearby galaxy.

There are 7 stars (Table D.1) with 160 μm significance χ_{160} > 3.0; 2 of them also have 100 μm significance χ_{100} > 3.0. However, the genuineness of those excesses are questionable since there are extended, background structures or nearby bright objects which impact on the reliability of the 160 μm estimates. A description of these objects with contourplots and images is given in Appendix D. Summarizing these two last paragraphs, the stars HIP 40693, HIP 72603, and HIP 82860 are listed in Table 12 as non-excess stars with *Herschel*, while the 7 stars in Table D.1 (included the mentioned HIP 40843) are neither considered excess stars because their χ values larger than 3 are questionable.

7.1.1. Dust luminosity upper limits of non-excess sources

Upper limits of the dust fractional luminosities, $L_d/L_\star$, of the non-excess sources are given in Table 12. Those values have been estimated from the 3σ statistical uncertainty of the 100 μm

flux using the expression (4) by Beichman et al. (2006) and assuming a black body temperature of 50 K, which is a representative value for 100 μm. Figure 7 presents a histogram of the $L_{dust}/L_\star$ upper limits. The mean and median values of these upper limits are 2.0×10^{-6} and 1.6×10^{-6}, respectively. There are 19 stars (8 F-type, 6 G-type, and 5 K-type) out of the 95 non-excess stars with $L_d/L_\star$ < 10^{-6}, i.e., a few times the EKB luminosity. The two stars with the lowest upper limits, $L/L_\star$ < 5.0×10^{-7}, are located at distances less than 6.1 pc, i.e. they are very nearby stars (HIP 3821 and HIP 99240). These upper limits represent an increase in the sensitivity of around one order of magnitude with respect to the detection limit with *Spitzer* at different spectral ranges (e.g. Trilling et al. 2008; Lawler et al. 2009; Tanner et al. 2009).

Figure 8 presents the $L_d/L_\star$ upper limits as a function of the effective temperature of the stars, i.e., spectral types (top plot) and of the distance to the stars (middle plot). Similar plots have been presented by Trilling et al. (2008) and Bryden et al. (2009). Our plots show that while the $L_d/L_\star$ upper limits tend to increase for the later K-type stars, the closer stars have low upper limit values, irrespectively of their temperatures. The bottom plot of Fig. 8 reflects that the flux contrast between the stellar photosphere and a potentially existing debris disc is determined by the bias introduced simultaneously by the distances and spectral types.

7.2. Excess sources

A total of 31 out of the 133 DUNES targets show excess above the photospheric predictions: 9 F-type, 12 G-type and 10 K-type stars (Table 13). The excess sources with the estimated PACS fluxes, the photospheric predictions and the significance of the excess at each PACS band are listed in Table 14. We also include the MIPS70 μm flux of each object. In general PACS70 and MIPS70 fluxes are in good agreement, although in the case of HIP 4148 the larger MIPS excess is likely due to contamination by nearby objects. Figure 6 shows χ_{100} and χ_{160} histograms of the excess sources (up to the value of 20). Stars with χ_{100} < 3.0 correspond to the cold disc candidates (see below Sect. 7.2.4), while stars with χ_{160} < 3.0 correspond to the steep SED sources (see below section 7.2.5). Figure E.1 shows the observed SEDs of the stars. The number of excess sources detected with *Herschel* data reflects an increase of 10 sources with respect to the number of previously known 70 μm MIPS *Spitzer* excess sources (HIP 72603 is excluded since it does not have a 70 μm excess with *Herschel*). We note again that HIP 40693 is a 24 μm warm excess, but without 70 μm excess; this object is not listed in Table 14. HIP 171 has been reported as having an excess at 24 μm but no 70 μm MIPS excess (Koerner et al. 2010); in this case, we consider it as a new detection. We note that most of the new excess sources are K-type stars; this trend clearly reflects the higher sensitivity of *Herschel* to detect lower contrast ratios between the stellar and dust-disc fluxes, particularly at 100 and 160 μm.

In order to cleanly assess the increase of the incidence rate provided by *Herschel* with respect to *Spitzer*, we note that the figures of the previous paragraph are biased since we selectively included 9 stars between 20 and 25 pc with planets and/or *Spitzer* debris discs in the 133 DUNES sample (see Sect. 3). Correcting the figures from this bias, i.e., considering the 20 pc DUNES sample of 124 stars, and also taking into account that the *Spitzer* excess of HIP 72603 is not supported by our PACS data, the number of previously known stars with *Spitzer* excesses at 70 μm is 15, while the total number of *Herschel* excess
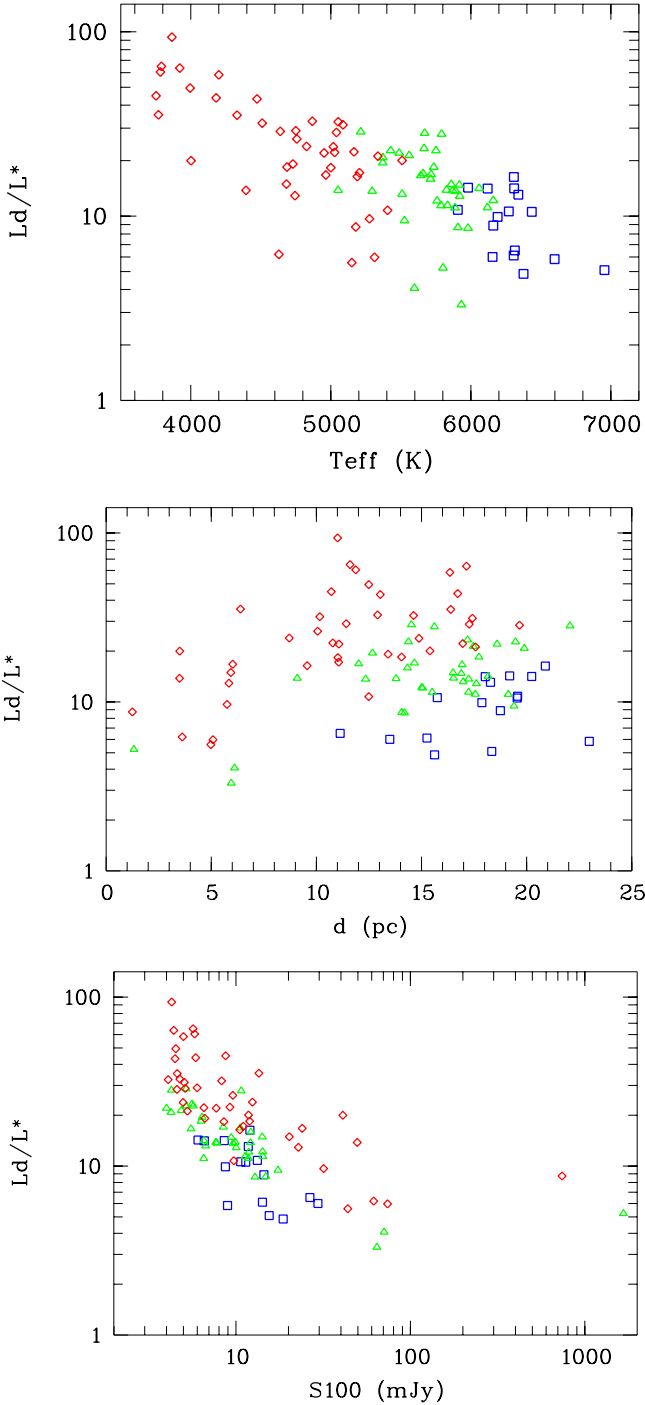
Fig. 8. Upper limit of the fractional luminosity of the dust (units: 10^{-7}) for the non-excess sources versus effective temperature of the stars (*top*), distance (*bottom*) and stellar flux (*bottom*). Blue squares: F-type stars; green triangles: G-type stars; red diamonds: K-type stars.

sources, either at 100 and/or 160 μm, are 25. This represents an increase of the incidence rate from the *Spitzer* 12.1% ± 5% to the *Herschel* 20.2% ± 2% rate, i.e., around 1.7 times larger. The gain in the debris disc incidence rate varies very much with the spectral type. The 20 pc DUNES sample is formed by 20 F-type stars, 50 G-type stars and 54 K-type stars. According to spectral types, the *Spitzer* discs are surrounding 2 F-type stars (~10.0%), 9 G-type stars (~18.0%) and 5 K-type stars (~9.3%). The same values for *Herschel* are: 4 (20.0%) for the F-type stars, 11 (22%) for the G-type stars and 10 (18.5%) for the K-type

stars (Table 14). We note that the fraction of stars with *Spitzer* excesses in our sample is a bit lower than what has been found in different FGK star programmes specifically focused to detect debris discs with the *Spitzer*/MIPS photometer (e.g. Trilling et al. 2008; Hillenbrand et al. 2008). This is possibly due to the highest spatial resolution of our *Herschel* images, which partly avoids the contamination suffered by the largest *Spitzer* beam.

The results described in the previous paragraph point to an incidence rate of debris discs around main-sequence, solar-type stars of around 20%, irrespectively of spectral type. This result can be considered as a lower limit to the true number of such discs and it must be taken very cautiously since it is affected by different sorts of biases, as well the previous ones with *Spitzer* were. We have shown in Sect. 7.1.1 how the $L_{\rm d}/L_{\star}$ upper limit depends on the combined effect of the stars' spectral types and distances. This is a strong bias clearly penalizing late type stars at distances larger than around 10 pc (see Fig. 8). In addition, our 20 pc sample is not complete for K-type stars for distances larger than around 15 pc due to HIPPARCOS completeness. If we restrict the DUNES sample up to 15 pc to avoid this incompleteness, our incidence rate is strongly affected, mainly with respect to the F-type stars. The reason is that most of the nearby F-type stars are bright enough to detect the stellar photosphere with the shallower DEBRIS integration time and, according to the DUNES/DEBRIS agreement, those stars have been observed by that *Herschel* OTKP.

7.2.1. Background contamination and coincidental alignment

Some of the PACS images reveal large scale field structures denoting the presence of interstellar cirrus. Good examples are some stars located close to the galactic plane like HIP 71683/81 (α Cen A/B), HIP 124104/07 (61 Cygni A/B) or HIP 71908 (α Cir). These structures make it difficult to estimate reliable PACS fluxes and even can mimic an excess over the predicted photospheric flux (see Appendix D for some examples).

In addition, as indicated before, the PACS 100 and 160 μm images are very sensitive to background objects. Therefore, the possibility of coincidental alignment of such sources with our stars, hindering a reliable flux measurement or artificially introducing an excess, cannot be excluded. To assess this potential contamination one needs to take into account the correlation between the optical and *Herschel* positions, the photospheric predictions at the different wavelengths and the *Herschel* observed fluxes, as well as the density of extragalactic sources. HIP 82860 is a concrete example of such a case of contamination. The estimated 100 μm flux agrees well with the predicted photospheric flux (Table 12) but we cannot reliably measure the 160 μm flux due to the presence of a bright, red background galaxy (42.2 and 56.0 mJy at 100 and 160 μm, respectively) located at a distance of ~10″ from the star (Fig. 9). That distance and the 160 μm ratio between the star and the galaxy (the 160 μm predicted flux of HIP 82860 is 5.5 mJy) prevent us from resolving both objects, even using deconvolution techniques. Further examples of such potential contamination by extended structures or background galaxies are presented in Appendix D, where PACS images of seven objects with significances $\chi 160 > 3$ (some cases also with $\chi 100 > 3$) are described. We remark that none of those objects are identified as excess sources in this work.

Nonetheless, we need to evaluate the impact of contamination by coincidental alignment in our identified debris disc stars. In the following we make some probabilistic estimates to quantitatively assess the chances of misidentifications of background

Table 14. Excess sources.

HIP	SpT	PACS70 (mJy)	S70 (mJy)	χ_{70}	PACS100 (mJy)	S100 (mJy)	χ_{100}	PACS160 (mJy)	S160 (mJy)	χ_{160}	$L_d/L_\star$	T_d (K)	R_d (AU)	MIPS70 (mJy)	Notes
171	G3V		22.90 ± 0.44		11.70 ± 1.26	11.22 ± 0.21	0.38	12.48 ± 2.36	4.38 ± 0.08	3.43	≤21.6e-06	≤25	≥ 97.1	44.10 ± 13.63	H, p, c
544	K0V		15.24 ± 0.34		54.12 ± 1.00	7.47 ± 0.17	47.15	23.03 ± 2.06	2.92 ± 0.07	9.86	4.8e-05	90	7.5	102.6 ± 7.83	e
4148	K2V	13.66 ± 1.37	8.98 ± 0.13	3.42	11.33 ± 1.17	4.40 ± 0.06	5.92	15.64 ± 1.72	1.72 ± 0.02	8.09	9.4e-06	32	41.2	37.10 ± 6.59	p
7978	F8V	896.20 ± 26.90	17.48 ± 0.99	32.67	897.10 ± 26.90	8.56 ± 0.48	33.03	635.90 ± 31.80	3.35 ± 0.19	19.89	3.1e-04	60	26.6	863.4 ± 58.68	e
13402	K1V		20.72 ± 0.37		51.77 ± 1.11	10.15 ± 0.18	37.50	36.94 ± 2.94	3.97 ± 0.07	11.21	1.7e-05	52	17.9	67.70 ± 7.06	e
14954	F8V		26.43 ± 1.17		39.45 ± 1.75	12.95 ± 0.58	15.14	31.75 ± 1.16	5.06 ± 0.22	23.01	4.2e-06	40	95.0	42.50 ± 4.76	e, !
15371	G1V	44.50 ± 2.50	25.78 ± 0.33	7.49	40.40 ± 2.50	12.63 ± 0.16	11.11	42.60 ± 2.50	4.93 ± 0.06	15.07	1.0e-05	40	47.7	45.40 ± 4.95	e
17420	K2V	15.99 ± 1.81	9.36 ± 0.13	3.66	14.79 ± 0.84	4.58 ± 0.06	12.15	10.65 ± 1.30	1.79 ± 0.03	6.82	9.2e-06	45	20.7	23.60 ± 5.44	H, p, s
17439	K1V	74.80 ± 4.10	8.61 ± 0.14	16.14	75.00 ± 4.20	4.22 ± 0.07	16.85	74.60 ± 4.70	1.65 ± 0.03	15.52	8.1e-05	48	21.3	88.50 ± 7.46	e
22263	G3V		21.13 ± 0.38		77.60 ± 2.00	10.35 ± 0.18	33.62	47.00 ± 3.00	4.04 ± 0.07	14.32	2.9e-05	70	15.4	113.6 ± 8.53	e
27887	K3V	14.60 ± 1.43	10.01 ± 0.19	3.21	8.05 ± 0.95	4.90 ± 0.10	3.32	8.02 ± 1.50	1.92 ± 0.04	4.07	3.8e-06	29	46.2	17.20 ± 4.94	H, p
28103	F1V		56.33 ± 0.31		45.46 ± 1.42	27.60 ± 0.15	12.58	9.37 ± 1.84	10.78 ± 0.06	−0.77	6.3e-05	100	18.3	93.90 ± 7.76	p, s
29271	G5V		35.50 ± 0.42		17.80 ± 1.30	17.40 ± 0.21	0.31	14.35 ± 2.00	6.80 ± 0.08	3.78	≤29.7e-06	≤22	≥147.3	42.60 ± 10.50	H, e, c
32480	G0V	264.00 ± 4.10	22.33 ± 0.27	58.94	252.30 ± 3.18	10.94 ± 0.13	75.90	182.09 ± 3.77	4.27 ± 0.05	47.17	6.9e-05	60	28.5	262.8 ± 18.29	e
42438	G1.5Vb		18.12 ± 0.25		17.31 ± 0.80	8.88 ± 0.12	10.54	6.73 ± 2.04	3.47 ± 0.05	1.60	1.1e-05	99	7.8	41.20 ± 4.16	p, s
43726	G3V		13.48 ± 0.26		15.77 ± 0.76	6.60 ± 0.13	12.07	6.09 ± 1.42	2.58 ± 0.05	2.47	1.6e-05	99	7.9	32.50 ± 4.13	p, s
49908	K8V		55.55 ± 2.11		22.50 ± 0.90	24.59 ± 1.03	−2.33	16.00 ± 1.70	9.61 ± 0.40	3.16	≤21.6e-06	≤22	≥ 56.6	38.70 ± 4.69	H, e, c
51459	F8V		31.14 ± 0.53		19.71 ± 1.42	15.26 ± 0.26	3.13	9.17 ± 2.79	5.96 ± 0.10	1.15	9.1e-07	50	38.6	33.80 ± 4.43	H
51502	F2V		16.57 ± 0.22		47.25 ± 2.00	8.12 ± 0.11	19.57	72.45 ± 2.22	3.17 ± 0.04	31.21	1.3e-05	30	145.0	39.60 ± 3.79	e, !
62207	G0V		13.45 ± 0.11		55.06 ± 2.39	6.59 ± 0.05	20.28	44.49 ± 3.17	2.57 ± 0.02	13.22	2.1e-05	66	18.3	55.70 ± 5.20	e
65721	G5V		42.07 ± 0.36		40.73 ± 0.66	20.61 ± 0.17	30.48	26.97 ± 1.39	8.05 ± 0.07	13.61	3.8e-06	45	66.1	79.00 ± 8.09	p
71181	K3V	15.06 ± 1.30	9.98 ± 0.16	3.91	8.79 ± 1.00	4.89 ± 0.08	3.90	1.63 ± 1.63	1.91 ± 0.03	−0.17	8.0e-06	70	7.9	29.20 ± 8.04	H, p, s
72848	K2V		21.45 ± 1.06		19.60 ± 2.00	10.51 ± 0.52	4.55	13.30 ± 1.12	4.11 ± 0.20	8.21	2.8e-06	40	34.2	33.50 ± 6.41	H, e
73100	F7V		14.42 ± 0.23		13.84 ± 0.81	7.06 ± 0.11	8.37	12.46 ± 2.27	2.76 ± 0.04	4.27	2.7e-06	30	144.8	24.70 ± 3.17	p, c, !
85235	K0V		12.83 ± 0.19		34.70 ± 1.18	6.29 ± 0.09	24.08	28.00 ± 2.52	2.46 ± 0.04	10.13	2.0e-05	45	24.6	58.00 ± 4.92	e
92043	F6V	59.00 ± 3.50	48.70 ± 0.68	2.94	30.20 ± 2.40	23.90 ± 0.33	2.63	21.90 ± 3.80	9.34 ± 0.13	3.31	7.0e-07	30	213.3	69.80 ± 8.93	H, e, c
103389	F7V	44.00 ± 2.30	13.45 ± 0.23	13.28	26.30 ± 1.70	6.59 ± 0.11	11.59	7.70 ± 2.50	2.57 ± 0.04	2.05	1.7e-05	90	13.6	46.60 ± 4.93	p, s, !
107350	G0V		12.51 ± 0.17		15.10 ± 1.30	6.13 ± 0.08	6.90	4.40 ± 2.30	2.39 ± 0.03	0.87	1.2e-05	100	8.1	28.40 ± 3.15	p, s
107649	G2V	284.00 ± 1.50	18.38 ± 0.20	177.0	311.00 ± 1.00	9.01 ± 0.10	301.9	211.00 ± 1.50	3.52 ± 0.04	138.3	1.0e-04	55	28.7	278.2 ± 21.46	e
109378	G0		9.51 ± 0.13		8.50 ± 1.00	4.66 ± 0.07	3.84	12.40 ± 1.60	1.82 ± 0.03	6.61	5.4e-06	22	160.2	7.90 ± 2.26	H, p, c, !
114948	F7V		14.08 ± 0.19		40.80 ± 1.60	6.90 ± 0.09	21.19	13.30 ± 2.20	2.69 ± 0.04	4.82	2.7e-05	90	13.1	68.70 ± 5.51	p, s, !

Notes. PACS fluxes (PACS.l) together with the photospheric predictions (S.l) and the significance at each band. The fractional luminosities and the black body temperatures and radii of the dust are also given as well as *Spitzer* fluxes at 70 μm. Column Notes: H = new *Herschel* debris disc, p = point-like object, e = resolved object, c = cold disc, s = steep source, ! = stars of the 20–25 pc subsample.
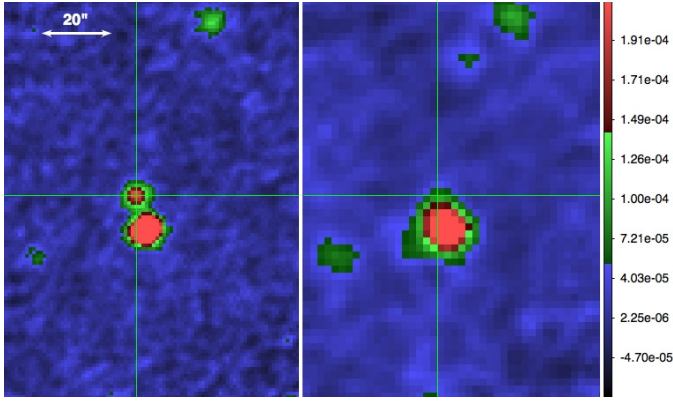
Fig. 9. PACS 100 (*left*) and 160 μm (*right*) images of HIP 82860. The crosshair denotes the position of the 100 μm flux peak. The angular scale is shown in the 100 μm image by a 20$''$ segment. Flux scale units are Jy/pixel. North is up and east to *the left*.

objects with debris discs. We follow the results obtained by Berta et al. (2011), who studied the cosmic infrared background in a few large areas of the sky and carried out number counts, i.e., source densities, in the PACS bands and flux range from $\sim$1 mJy to few hundreds mJy. This is the range of interest for our observations. We base our estimates on Fig. 7 of Berta et al. (2011), which provides differential number counts per square degree for the PACS bands in the GOODS-S field. We firstly note that many of our identified *Herschel* debris discs have very large excesses, several tens of mJy in the PACS bands, and that some of them even show IR excess emission over the photosphere in the mid-IR wavelength range of the *Spitzer* IRS instrument (see Fig. E.1). In those cases, the probability of confusion due to background objects is practically negligible. The problematic misidentifications arise for those with low excesses at 160 μm, of the order of few mJy, with small $\chi 160$ values and very low or non-excess at 100 μm. Specifically we identify 6 objects (Table 14): HIP 171, HIP 27887, HIP 29271, HIP 49908, HIP 92043, and HIP 109378. The 160 μm differential number counts for sources with flux level $\sim$5–6 mJy from Fig. 7 of Berta et al. (2011) is $\sim$2000 sources per square degree and mJy, while for fluxes $\sim$12–13 mJy is $\sim$400 sources per square degree and mJy. This flux range recovers the observed excesses of the above objects. The size of the sky area to estimate the density of sources is taken as the one for which two different objects can be resolved. In this respect, we note that α Cen A and B with flux ratio of about 2 and a separation of $\sim$3$''$1 on the PACS 100 μm images can clearly be distinguished, but not at 160 μm. In parallel, we have introduced two fake objects with the same flux, 7 mJy, at different angular separations in the PACS 100 μm and 160 μm images of one of our fields. Using a 2D Gaussian treatment we could recover both fake objects at angular distances of 3$''$ and 5$''$ at 100 and 160 μm, respectively. These figures are consistent with the α Cen observational result and slightly smaller than the *Herschel* beam sizes. Thus, taking the conservative approach of the source density for the lowest excess, 0.0121 is the number of 160 μm sources in a field of area corresponding to the estimated angular separation, which implies that the probability of a coincidental alignment of a background galaxy is 1.2%. Considering the 133 DUNES stars, the binomial probability that all six objects mentioned above are background galaxies is just 0.4%, however the chance that one is a false disc detection is 32%.

We note that the estimated probabilities depend on a number of assumptions. The main one is to assume that all DUNES fields have equal source densities as the GOODS-S field. This is simply not true since the number counts change significantly from field to field. However, Sibthorpe et al. (2012) have found no statistically significant cosmic variance based on 100 μm data from the DEBRIS survey; further, assuming that this result is also valid at 160 μm and flux levels below the DEBRIS detection limit, they estimate a confusion probability based on the Berta et al. (2011) 160 μm data which is in excellent agreement with our own estimate above. Thus, we conclude that the probability that all faint debris discs in Table 14 are background galaxies is rather low, although we certainly cannot exclude false identifications. At present we cannot distinguish between real cases and false alarms, although some observational prospectives can be traced (Krivov et al. 2013). On the other hand, a detailed analysis of the number counts and the source density in the DUNES fields as a function of flux levels, colours and the galactic latitude will be published in a forthcoming paper (del Burgo et al., in prep.).

7.2.2. Dust properties

The excess infrared emission from the debris discs originates in small dust grains produced in collisions of large bodies. A common approach to estimate the temperature and the irradiated luminosity of those grains is to assume that they behave as black body grains. This approach also allows us to estimate a representative orbital distance of the black body-like dust (Backman & Paresce 1993). This procedure presents several caveats. Observed SEDs of some discs clearly reveal the presence of dust at multiple temperatures (e.g. Hillenbrand et al. 2008; Lawler et al. 2009). A simple look at the SEDs presented in Fig. E.1 suggests a range of temperatures of the dust. This can either be due to its location at a range of distances from the star or to dust at the same distance but with different properties. It has already been mentioned the well known fundamental degeneracy between distance and size of the dust particles, as small grains far from the star can produce the same SED as large grains located close in (Krivov 2010). At this point we note that the distribution of dust over a radial range has directly been proven by spatially resolved imaging in scattered and reemitted radiation (e.g. Ertel et al. 2011).

Nevertheless, the simple black body assumption still provides a reasonable approach for most of the debris discs and for comparison among solar-type stars, although the black body radius underestimates the true one (e.g. Wyatt 2008; Ertel et al. 2012b, and references therein). Based on these, black body temperatures, T_d, have been estimated by fitting a black body for those sources with excesses at several bands. Where the excess is observed only at one band, mainly at 160 μm, the upper limit of the temperature is given. The fractional luminosity of the dust has been estimated integrating the observed excess fluxes; in those cases with excess at one wavelength, we have used the expression (4) of Beichman et al. (2006) assuming a dust temperature of 50 K. The orbital distance at which the dust would be located is estimated following Eq. (3) from Backman & Paresce (1993). In general, for those objects previously known as debris discs, the dust properties obtained using the *Herschel* data do not differ significantly from those obtained with *Spitzer* (e.g. Beichman et al. 2006; Trilling et al. 2008). The calculated values for the mentioned three dust parameters are given in Table 14. $L_d/L_\star$ spans approximately two orders of magnitude, $\sim$7$\times$10^{-7}– 3$\times$10^{-4}, and are in a few cases very close to the sensitivity limit.

Table 15. Stars associated with extended emission.

HIP	Position angle	Observed diameters (arcsec)	$FWHM_c$ (arcsec)	$FWHM_G$ (arcsec)	Band
544	102°	18.0,16.0	8.8,7.8	8.67 ± 0.10, 8.28 ± 0.10	100 μm
7978	51°	39.0,28.0	15.7,11.3	15.5 ± 0.02, 9.02 ± 0.02	100 μm
13402	50°	19.0,14.0	9.2,6.7	8.20 ± 0.10, 7.61 ± 0.02	100 μm
14954(!)	30°	18.0,14.0	9.4,7.3	9.89 ± 0.10, 7.80 ± 0.10	100 μm
15371	98°	39.0,18.0	24.5,11.6	20.00 ± 1.0, 12.20 ± 0.36	160 μm
17439	105°	26.0,14.0	13.1,7.1	13.35 ± 0.14, 8.68 ± 0.10	100 μm
22263	5°	21.0,16.0	10,7.6	10.20 ± 0.10, 8.41 ± 0.09	100 μm
29271	70°	16.0,10.0	14.3,8.9	12.00 ± 1.22, 10.00 ± 0.73	160 μm
32480	107°	34.0,20.0	16.0,9.4	17.76 ± 0.07, 10.15 ± 0.04	100 μm
49908	50°	18.0,10.0	15.5,8.6	13.00 ± 0.94, 11.00 ± 0.60	160 μm
51502(!)	0°	16.0,16.0	8.3,8.3	9.08 ± 0.12, 8.10 ± 0.11	100 μm
62207	130°	24.0,14.0	13.4,7.8	13.13 ± 0.19, 8.40 ± 0.11	100 μm
72848	75°	21.0,12.0	12.7,7.2	11.07 ± 0.33, 6.64 ± 0.20	100 μm
85235	0°	18.0,16.0	10.2,9.0	10.01 ± 0.23, 9.21 ± 0.21	100 μm
92043	170°	16.0,10.0	19.1,11.9	14.00 ± 1.10, 10.00 ± 0.79	160 μm
107649	125°	17.5,8.0	16.1,11.2		100 μm

Notes. Column 2 gives the position angles on the sky (from north to east). Column 3 gives the elliptical diameters (major,minor) of the 3σ contours. Column 4 ($FWHM_c$) gives the x and y FWHM values assuming the 3σ contours are Gaussian, while Col. 5 ($FWHM_G$) is a 2D Gaussian fit to the whole detected flux. See text for details. The last column gives the wavelength at which the sizes have been estimated. (!) Stars of the 20–25 pc subsample.

The new *Herschel* discs tend to be approximately one order of magnitude fainter than the previously known ones, mean values are ~4×10^{-6} against ~4×10^{-5}, respectively (Table 14). T_d values range ~20–100 K, with the lowest temperatures also mainly related to the new *Herschel* discs, mean value ~34 K against ~64 K. As expected, the black body radius tends to be larger for the *Herschel* discs, mean distance ~82 AU against ~38 AU. A short compendium of these results is that the new *Herschel* discs trace fainter and colder debris discs than the previously known discs.

7.2.3. Point-like and extended sources

Most of the known debris discs have been characterised by fitting the observed SEDs. Spatially resolved images help to break the inherent SEDs' degeneracies by showing where most dust is located. More than 30 debris discs are known to be resolved[9]. Resolved imaging at different wavelengths serves not only to confirm the presence of circumstellar discs, but provides important constraints to their properties, like the dust location and reliable temperatures. Furthermore, resolved discs display features as warps, clumps, rings, asymmetries, etc., which help in the study of the dynamics of the discs and indirectly prove the presence of planets (Wyatt 2008, and references therein).

The *Herschel* PACS observations reveal a large number of stars associated with extended emission at 100 μm and/or 160 μm. Their 3σ flux contours usually show an elliptical-like shape. The size of the extended sources is estimated by fitting ellipses to the 3σ contours of each source by eye. Columns 2 and 3 of Table 15 gives the position angle (measured from north to east) and the elliptical 100 μm major and minor diameters. We estimate an uncertainty of ~1″ (i.e., 1 pixel at 100 μm). We have preferably chosen that wavelength due to the complexity of the surrounding fields at 160 μm in many of the objects. In the case of the HIP 29271, HIP 49908, and HIP 92043 their sizes are given at 160 μm because they are cold disc candidates (see Sect. 7.2.4). To assess if the 3σ contours truly denote

extended emission, we proceed in the following manner. Firstly, we have assumed that the source brightness profile is well approximated by a Gaussian and measured the ratio between the peak flux and the 3σ flux values, assuming that this ratio corresponds to a Gaussian at a distance from the center given by the semiaxes of the ellipses representing the 3σ contours. In this way we have estimated the FWHM of the emission in both axes (Col. 4 of Table 15). Secondly, we have carried out a two-dimensional Gaussian analysis of the sources using the IDL procedure MPFIT2DPEAK, fitting the observed brightness profiles with a rotated 2-D Gaussian profile weighted by the uncertainties, without applying any prior assumption as regards the shape of the emission (Col. 5 of Table 15). Both methods yield quite consistent results within the uncertainties. Thirdly, once we have the Gaussian sizes we need to evaluate whether they reflect truly extended emission. FWHM values of the *Herschel* PACS PSFs are ~7″ and 12 ″ at 100 μm and 160 μm, respectively, but small variations of the PSF due to the brightness of the sources and the observing strategy are known to exist (Kennedy et al. 2012). In order to assess if the sources are resolved, a Monte-Carlo simulation has been carried out taking as reference HIP 544 and HIP 72848, two relatively faint sources with small FWHM values, which in the case of HIP 72848 is only resolved in one direction. The standard star α Boo is taken as representative of a pure point-like PSF. The 100 μm PACS image of α Boo has been rotated so that the new x and y axes correspond to the axes of the extended emission, and its PSF has been scaled to the flux of each star. The new α Boo PSF has been inserted in a grid of 2627 and 1568 locations in the cleanest areas of the HIP 544 and HIP 72484 images. For each position the x and y FWHM values have been estimated using a 2D Gaussian fit. This provides the FWHM distribution of point sources with the same flux as the problem objects over a noisy background. No additional noise has been added to the images because the telescope thermal noise and sky confusion, already included in the frames, are much larger than the Poisson contribution for such faint artificial sources. The distributions of the FWHM values obtained with both Monte-Carlo simulations are approximately Gaussian. Thus, by using both Gaussian statistics and the

---

[9] http://www.circumstellardisks.org

empirical distributions constructed above we can estimate the probability that a point source randomly provides the FWHM values listed in Table 15. The result is that the probability of false positives seems below 0.1%. Since HIP 544 and HIP 72484 are among the most unfavourable cases, we conclude that the extended nature of all objects identified as such in Table 15 is fairly secure. We point out that Kennedy et al. (2012) also claim to have resolved a disc with a FWHM of 8″.2 × 6″.9.

The number of sources listed in Table 15 associated with extended emission is 16, i.e., ∼52% out of the 31 excess sources. This represents a huge increase of resolved discs with respect to the 3 sources in our sample previously resolved with *Spitzer* or any other facility (HIP 7978, HIP 32480, HIP 107649). Disc size values in Table 15 are upper limits, since proper deconvolution is required to estimate more realistically the true extension of the debris discs and their structure. This has already been done for some of the sources for which a deeper observational analysis (Liseau et al. 2010; Eiroa et al. 2011; Marshall et al. 2011) or highly detailed modelling (Löhne et al. 2012) has been carried out. Similar work is in progress for a few more sources (Marshall et al., in prep.; Stapelfeldt et al., in prep.; Faramaz et al., in prep.).

7.2.4. Cold disc candidates

Some of the identified debris disc sources in Table 14 show an excess at 160 μm but little or no excess at all at 100 μm. These sources are HIP 171, HIP 29271, HIP 49908, HIP 73100, HIP 92043, and HIP 109378. We note that the 100 and 160 μm source positions agree within the astrometric errors. The infrared excesses have been attributed to a new class of cold, debris discs, characterized by low temperatures, ≲30 K, and low fractional luminosities (Eiroa et al. 2011). While it cannot be excluded that they suffer from background contamination, i.e., they might not be true circumstellar discs, the probability that one or more of these discs are real is large (Sect. 7.2.1). If true, the nature of these faint, cold discs cannot be explained by simply invoking the "classical" collisional models of debris discs. Alternative scenarios have been explored by Krivov et al. (2013). They argued that such discs might be composed of nearly unstirred primordial grains with sizes somewhere in the millimeter to kilometer range, which would imply that planetesimal formation has stopped before "cometary" or "asteroidal" sizes were reached, at least in the outer regions of the systems. Discs of this kind would experience low-velocity collisions without any significant production of small, warm grains. As a result, a bulk of the material would have a nearly black body temperature as suggested by the observed SEDs.

7.2.5. Steep SED sources

Some stars in Table 14 show an SED with the largest excess at 70 μm and a decrease with the wavelength at 100 and 160 μm. The stars with this behaviour are: HIP 28103, HIP 42438, HIP 43726, HIP 71181, HIP 103389, HIP 107350 and HIP 114948 (Fig. E.1). In some of these stars, the observed flux at 160 μm does not exceed the photosphere, i.e., the significance of the observed fluxes is ≤3, and the spectral index of the excess is steeper than the one corresponding to a black body in the Rayleigh-Jeans regime. The IR excesses are already noticeable in the wavelength range of the IRS instrument of *Spitzer* in all cases. All are point-like sources at 100 μm, which implies FWHM sizes ≲90–140 AU, depending on the distance to the

star. The morphology of the excess with well defined start- and end-wavelengths suggests, in principle, that the dust is confined in a well defined narrow ring.

Ertel et al. (2012a) made a detailed analysis of this behaviour and demonstrated that the particular SED of the discs provides strong constraints on the dust properties. They showed that the naively expected narrow ring shape of the disc is not very well constrained by the modelling, and found that the steep decrease of the SED is inconsistent with a power-law exponent of the grain size distribution of –3.5, expected from a standard equilibrium collisional cascade (Dohnanyi 1969). In contrast, a steeper grain size distribution or, alternatively, an upper grain size in the range of few tens of micrometers would be implied. This suggests a strong underabundance of large (millimeter-sized) grains to be present in the discs. Donaldson et al. (2012) recently presented another debris disc showing a similar behaviour, namely HD 3003. This disc, however, is significantly younger and more massive than the discs found in our survey and challenges the scenarios suggested by Ertel et al. (2012) to explain the phenomenon. An alternative scenario of enhanced stirring of the planetesimal disk by the companion star of HD 3003 has been proposed.

7.2.6. Short description of individual objects

As it has already been pointed out, a detailed description of individual stars or groups of stars is beyond the scope of this paper. Detailed observational and/or modelling analysis of some sources have been the subject of previous DUNES works (papers already mentioned), and there are some more papers in preparation. However, in order to partly illustrate here the achieved results, we present a brief description together with the *Herschel* images and contour plots of HIP 13402 and HIP 14954 (Fig. 10), two stars associated with resolved emission. The SEDs of these stars are included in Fig. E.1.

HIP 13402. This K1 V star is located at a distance of 10.35 pc and is one of the youngest stars in our sample, ∼130–400 Myr (Table 4). Previously identified as a debris disc based on the 70 μm *Spitzer* flux (Trilling et al. 2008), the excess is clearly present at 100 and 160 μm but it has a modest fractional luminosity of the dust. The star appears slightly extended at 100 μm (Table 15) and at 160 μm, with a FWHM observed size at 160 μm 12″.7 × 11″.4 (Fig. 10). A quadratic subtraction of the stellar PSF gives an intrinsic size of 5″.4 × 2″.6, which corresponds to a projected semi-major axis of 28 AU, and therefore slightly larger than the black body radius (Table 14).

HIP 14954. This F8 star is located at a distance of 22.58 pc and is one of the debris discs preserved in the DUNES sample because it was already identified as such with *Spitzer*. The star hosts a gas giant exoplanet and also is the primary component of a physical binary. The age is not well constrained and is in the range of ∼1–5.7 Gyr. The fractional luminosity of the dust is among the modest values of our debris disc sample (Table 14).

8. Discussion

There are many works in the literature searching for potential correlations between the debris disc characteristics and the main properties of their associated stars -like metallicity, spectral type, or age-, the presence of exoplanets around the stars or if the stars are multiple systems (e.g. Habing et al. 2001; Rieke et al. 2005; Beichman et al. 2006; Trilling et al. 2008; Bryden et al. 2009; Rodriguez & Zuckerman 2012). This search is motivated because it might provide helpful hints to deepen in the knowledge
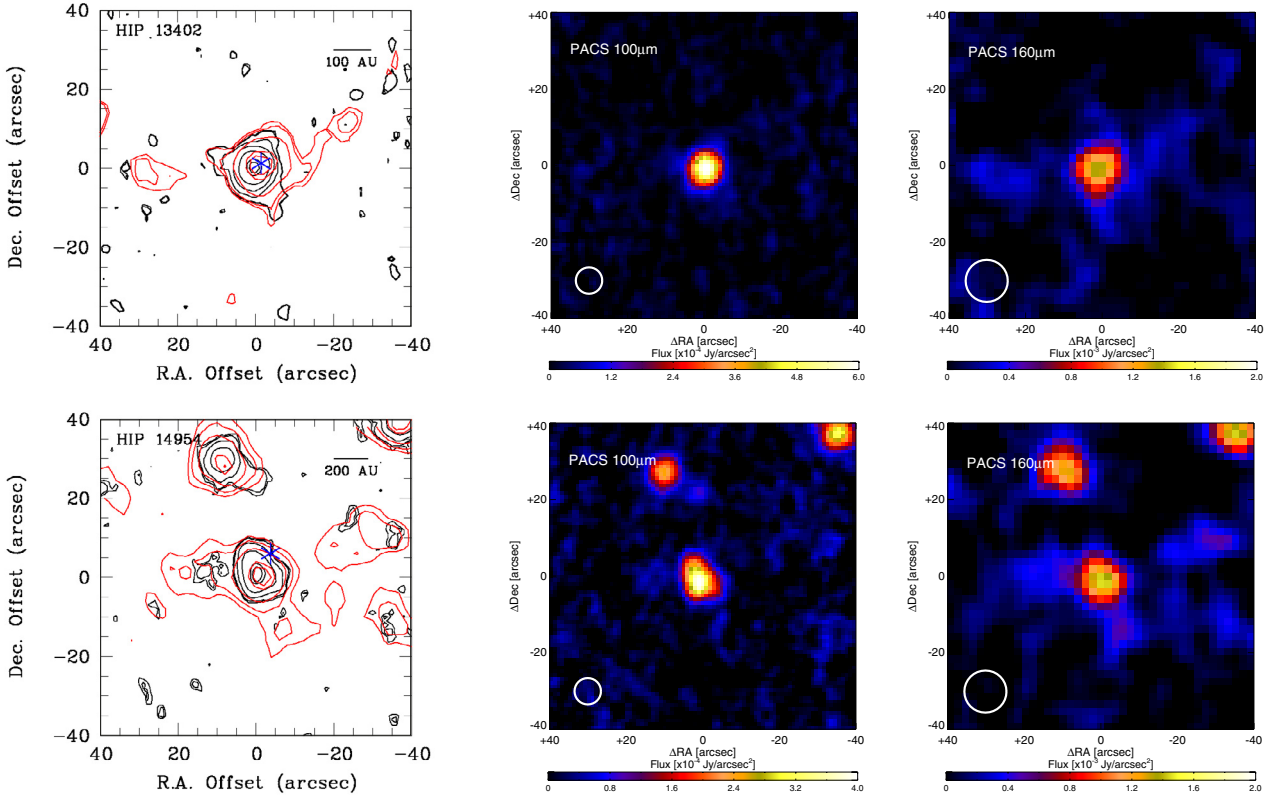
Fig. 10. Contours plots (*left*) and PACS 100 μm (*middle*) and 160 μm (*right*) images of two resolved debris disc stars. The identification of the stars are given in the *upper-left corner* of the contour plots. Position (0,0) refers to the 100 μm peak. The optical position of the stars with respect to the 100 μm peak is indicated by a "star" symbol. North is up and east *to the left*. Black contours correspond to 100 μm and red contours to 160 μm. HIP 13402: contours are 5%, 10%, 20%, 40%, 80%, 90% of the peak (100 μm), and 10%, 20%, 40%, 80%, 90% of the peak (160 μm). HIP 14954: contours are 10%, 20%, 40%, 80%, 90% of the peak at both bands. For both objects the lowest contour corresponds to 3σ.

of the conditions for the formation and evolution of planetary systems. In the following we revisit these analyses in view of the DUNES discs.

8.1. Debris discs/stellar metallicity

There exists a well established relationship between a high metallicity in solar-type stars and the incidence of extrasolar giant planets orbiting around them (e.g. Santos et al. 2004; Fischer & Valenti 2005), although such trend is not valid in the case of low mass planets, $M_p \lesssim 30\,M_\oplus$ (e.g. Ghezzi et al. 2010; Mayor et al. 2011). In the case of debris disc stars, the results from various works do not reveal any correlation between the presence of discs and the metallicity of the stars (e.g. Bryden et al. 2006; Trilling et al. 2008; Moór et al. 2011). The most recent and, to our knowledge, comprehensive study on this issue has been carried out by Maldonado et al. (2012) who, based on a set of homogeneously determined stellar parameters, analysed the metallicity distribution of different samples of stars. These samples included one of 107 solar-type stars with only debris discs and a control sample of stars without known debris discs and planets. They found that both samples have similar metallicity distributions, but there is a hint pointing out to a deficit of stars with discs at low metallicities or, in other words, stars with discs are slightly more metal rich than stars without discs (Figs. 3 and 7 of Maldonado et al. 2012). We have repeated this analysis for the DUNES stars, differentiating those with no detected disc emission and those with associated discs. We have removed from both groups the stars with known exoplanets in order to avoid a potential contamination. The average [Fe/H] for

the debris disc stars (26 objects) is -0.10 ± 0.18 and a median of -0.09, while for the non-excess stars the corresponding values are -0.15 ± 0.29 and -0.13, respectively. Thus, both metallicity distributions are practically undistinguishable. More conclusive statements require further data, in particular concerning the incidence of low-mass planets in debris discs systems, to confirm or unconfirm the mentioned hint, which might shed light on the conditions to form low mass planet and/or planetesimal systems (e.g. Bryden et al. 2006; Greaves et al. 2007; Moro-Martín et al. 2007, in prep.; Marshall et al., in prep.).

8.2. Disc properties/spectral types and bolometric luminosities

Figure 11 (top and middle rows) shows plots of the fractional luminosity of the dust, the black body radius and temperature versus the effective temperature and the bolometric luminosity of the stars. The dust parameters present a large scatter and the plots indicate that none of them are correlated with the effective temperatures and luminosities of the stars, as corroborated by Pearson or Spearman correlation tests. Average values of $L_d/L_\star$, T_d and R_d grouping the stars by their F, G and K spectral types agree within the high uncertainties involving these parameters. The only parameter that might be weakly correlated with the stars' spectral types is the estimated average black body radius, which might present a decrease with the spectral type: $\langle R_d \rangle = 79 \pm 74$ AU for the F-type stars, 53 ± 54 AU for the G-type, and 28 ± 16 AU for the K-type stars. The lack of a correlation between the fractional luminosity of the dust and spectral type is also seen in *Spitzer* studies (e.g. Trilling et al. 2008). We further
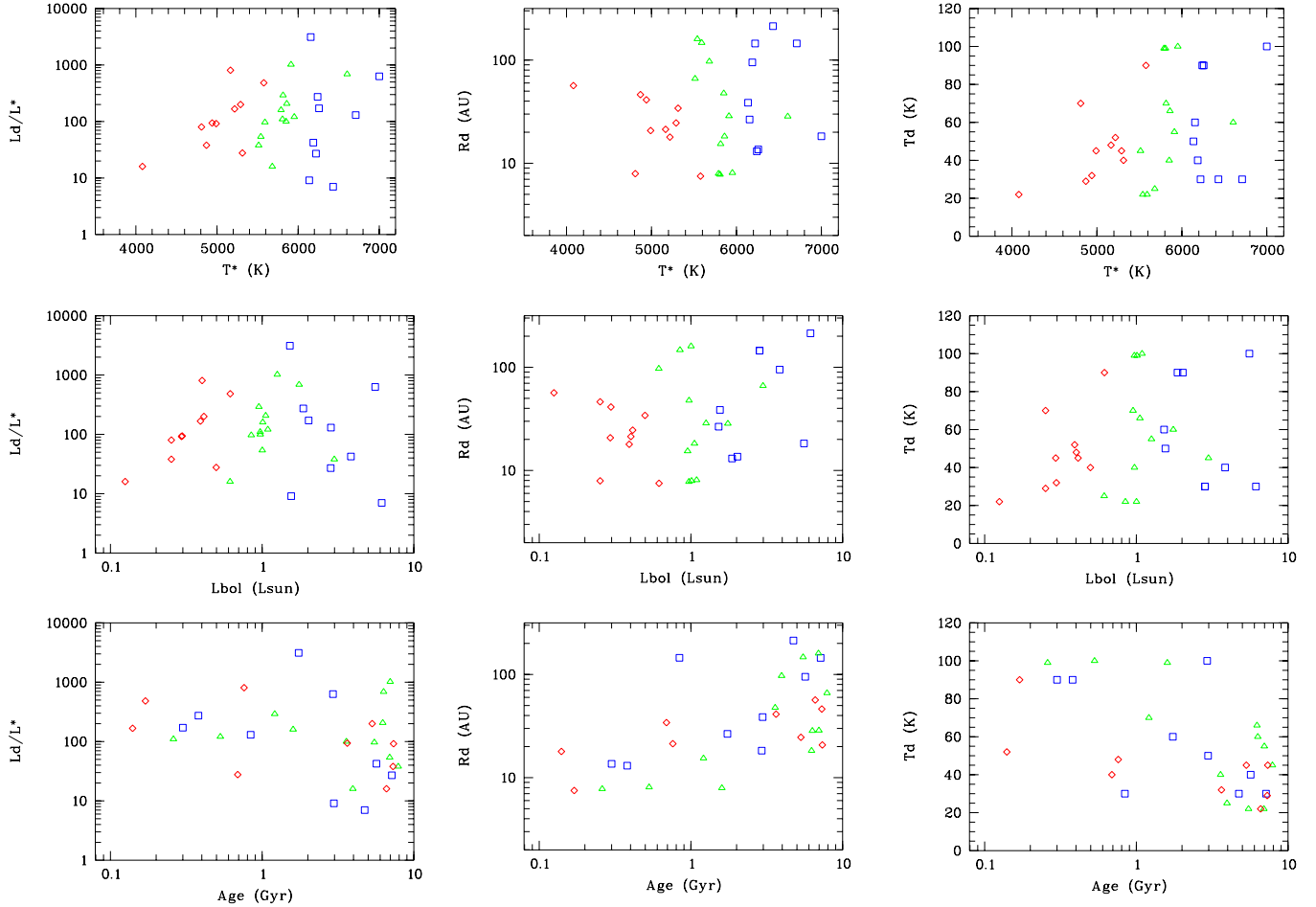
Fig. 11. Dust properties versus stellar effective temperature, bolometric luminosity and ages (based on the own Ca II activity index). Blue squares: F-type stars; green triangles: G-type stars; red diamonds: K-type stars. Units of the fractional luminosity of the dust are 10^{-7}.

note that, excluding q^1 Eri (HIP 7978), the range of $L_d/L_\star$ does not change much, although the disc detectability changes with the spectral type (Fig. 8). We also note the fact that the dust temperature does not change with the stars' spectral type is because the dust is located on average at decreasing distances for the later stellar spectral types. Although the relative values provided by the simple black body approach might be useful (Wyatt 2008) to provide a basic view of the discs, it might be misleading because realistic grain properties are not taken into account. A firm interpretation of our debris disc properties and their relation with the stars' characteristics requires detailed modelling, which is beyond the scope of this work.

8.3. Debris discs/stellar ages

Stellar age is one of the main basic stellar quantities but at the same time of the most difficult to reliably determine for main-sequence solar-type field stars. The theoretical Hertzsprung-Russell diagram is not very useful since isochrones pile-up for these spectral types. There is a handful of age diagnostics used as proxies (Mamajek & Hillenbrand 2008), but they can give conflicting results. However, the use of consistent age estimates circumvent this problem, at least partly (e.g. Rieke et al. 2005). From IRAS, ISO, and *Spitzer* studies it is known that debris discs persist around solar-type stars through very long timescales (Habing et al. 2001; Decin et al. 2003; Moór et al. 2006; Hillenbrand et al. 2008). The rate of debris discs and their dust luminosity seem to be relatively large up to ages

≲400–500 Myr. For older stars, there is a small but not quite obvious decline up to ages of several Gyr (Trilling et al. 2008; Wyatt 2008). For all ages, the scatter is large.

Figure 11 shows in the bottom panels the dust fractional luminosity, the black body radius and temperature of the excess sources as a function of the stellar ages. We have used our own reduced spectra (Martínez-Arnáiz et al. 2010; Maldonado et al. 2010, 2012) to estimate ages in a consistent manner using the Ca II R'_{HK} activity index (Mamajek & Hillenbrand 2008). Again there is a large scatter in $L_d/L_\star$ for the stars in the sample, in particular for ages larger than ~3 Gyr where the bulk of the stars is concentrated. With respect to R_d and T_d, although the values present a scatter, the plots suggest a weak correlation of R_d and an anticorrelation of T_d with the stellar age. These trends hold for the FGK stars as a whole and individually for each F, G and K spectral types. In fact, a Pearson correlation test shows that the probability of R_d and T_d to be correlated with the age of all FGK debris disc stars are ~97% and larger than 99%, respectively. The apparent correlation between R_d and stellar age might be a hint for dynamical inward-out stirring of debris discs.

8.4. Debris discs/stellar multiplicity

The number of DUNES stars with an entry in the catalogues of binary and multiple stars CCDM (Catalog of Components of Double and Multiple Stars), WDS (Washington Double Star Catalog, Mason et al. 2011, version 2012), and SB9 (The 9th Catalogue of Spectroscopic Binary Orbits, Pourbaix et al. 2004,

Table 16. Multiplicity of the excess sources.

HIP	Separation	Proj. dist. (AU)	R_d (AU)	Status
171	0.″83	10.1	≥97.1	Y
544				?
13402				?
14954	3.″3	74.5	95.0	Y
15371	310″	3729	47.7	Y
29271	3.″05			?
32480	36.″2			N
49908	165″			N
51459	120″	1534	38.6	Y
65721	286.″4			N
72848		0.52	34.2	Y
92043	12.″6			?
107350	43.″2	795	8.1	Y
107649	55″			N
114948				?

Notes. The separation refers to the angular distance to the closest identified companion. Column 4 with the black body radius of the dust is included with the purpose of a direct comparison. The column "Status" informs if the stars are true physical systems (Y), projected but no true binaries (N) or lack of sufficient information (?).

version 2012) is 83 which represents ∼62% of the sample. Not all entries correspond to real multiple systems. Out of these 83 entries, 15 correspond to stars identified as excess sources. Table 16 lists these stars, where the angular and linear distances with the closest companions are given for the cases where such information is available. In the last column on that table, the stars with true identified physical companions are given. This association is based on the proper motions and distances for HIP 14954, HIP 15371, HIP 51459. The stars HIP 171 and HIP 72848 are spectroscopic binaries with well determined orbital parameters (Bach et al. 2009; Halbwachs et al. 2003; Bonavita & Desidera 2007). HIP 107350 is accompanied by a substellar object with a mass in the brown dwarf regime (Luhman et al. 2007). HIP 29271 has a companion candidate (Eggenberger et al. 2007) but no further information. The optical companions of HIP 32480, HIP 49908, HIP 65721 and HIP 107649 have proper motions very different from the associated stars, so that they most likely are no real physical companions. There is no information to our knowledge, beyond the entry in one of the mentioned catalogues, for HIP 544, HIP 13402 and HIP 114948. As a summary, we can firmly identify 6 multiple systems out of 31 debris disc stars. This implies a rate of ∼20%, close to the one found by Rodriguez & Zuckerman (2012). Concerning the stellar or dust properties, the binary stars do not have any significant trend. We note that our numbers are not statistically significant enough to confirm or deny the claim by Rodriguez & Zuckerman (2012) of a lower fractional disc luminosity for multiple systems than for single stars.

The comparison of the binary separation and the location of the dust (Cols. 3 and 4 of Table 16) is informative to assess if the dust resides in stable orbits. The discs around HIP 15371, HIP 51459 and HIP 107350 are clearly circumstellar since all the binary systems are very wide, while the discs around HIP 171 and HIP 7248 are circumbinary. These discs are located in stable orbits (e.g. Trilling et al. 2007; Rodriguez & Zuckerman 2012, for a comparison with other debris discs). The only questionable case is HIP 14954, where the black body radius and binary separation are similar and place the dust in an unstable location

(Rodriguez & Zuckerman 2012). In order to assess stability issues of the debris discs versus the binarity of the stars, a specific study using realistic grain properties informing on plausible dust locations and temperatures is required.

8.5. Debris discs/planets

The number of known stars hosting exoplanets in the DUNES sample is 21. This figure includes HIP 107350 with a companion of mass $M_P = 16 \, M_J$, i.e., in the brown dwarf mass regime although it is listed in the Extrasolar Planets Encyclopaedia[10]. Six of these stars – HIP 7978, HIP 14954, HIP 27887, HIP 65721, HIP 107350, and HIP 109378 – have debris disc detected with *Herschel*. A further star, HIP 40693 has a warm disc (Beichman et al. 2005) but no excess in our images. HIP 27887 and HIP 109378 are new debris disc detections by *Herschel*. If we consider the 20 pc DUNES sample, the number of stars hosting planets is 16, out of which 4 have debris discs (HIP 107350 is not included). Thus, the incidence rate of debris discs among exoplanet hosts is 25% ± 5%, i.e., only marginally larger than the fraction of discs around stars irrespective of whether they host a planet. HIP 7978, HIP 107350 and HIP 109378 have been studied by Liseau et al. (2010), Ertel et al. (2012a) and Eiroa et al. (2011), respectively. All DUNES and DEBRIS stars hosting exoplanets, including the disc non-detections, currently are the subject of a detailed treatment in two papers in preparation (Marshall et al., in prep. and Moro-Martín et al., in prep.).

9. Summary and conclusions

The purpose of this paper has been to present the observational results of the *Herschel* Open Time Key Project DUNES. The stellar sample consisted of 124 main-sequence, nearby (distances less than 20 pc), solar-type FGK stars, plus 9 stars with previously known debris discs or exoplanets, located at distances between 20 and 25 pc. Infrared excesses have been detected around a total of 31 stars out of the 133 stars and 25 stars out of the 124 stars in the 20 pc subsample. This represents a total increase of 10 new debris discs with respect to the ones previously known in the whole sample, and an increase in the incidence of debris discs in the 20 pc subsample from 12.1% ± 5% to 20.2% ± 2%, i.e., around 1.7 times larger. The gain in incidence rate varies with the spectral type, being larger for the K-type stars. The achieved mean sensitivity is a function of stellar spectral type and distance, and the 3σ mean upper limit of the fractional luminosity of the dust for non-excess sources is $L_d/L_\star \sim 2.0 \times 10^{-6}$, with the lowest values $L_d/L_\star \lesssim 4.0 \times 10^{-7}$ corresponding to the closest stars. This is a gain of around one order of magnitude against the detection limit of *Spitzer*. Among the debris disc stars, a few of them show $L_d/L_\star$, a few times larger than the EKB value, albeit these disks are larger and colder than the predicted EKB dust disk.

The number of stars with spatially resolved emission is 16, which is a rate of 52% among the identified debris discs, and a huge gain with respect to the previously known resolved sources (3 objects). In addition, few sources show excess emission at 160 μm and very faint or no excess at 100 μm which is attributed to a new class of cold and faint debris discs. Although it cannot be excluded that some of these sources suffer from coincidental alignment with background galaxies, the probability that some of these cold disc candidates are true debris discs is very large.

---

[10] http://exoplanet.eu

In addition, we have found that some discs show far-IR spectral indexes steeper than the black body Rayleigh-Jeans index. Both types of cold and steep-SED debris discs cannot easily be accommodated to the classical equilibrium collisional cascade scenario of debris discs.

An analysis of the debris disc parameters with stellar properties shows a weak trend of a correlation of the black body dust radii (the location of the dust) and an anticorrelation of the dust temperatures with the stellar age. This trend holds for all FGK spectral types as a whole, and for each F, G and K spectral types separately. No other correlation is found with the (possible) exception of a hint showing a decrease of the average black body dust radii from the F to the K spectral type stars. In-depth observational and modelling analysis of the DUNES debris discs will be published elsewhere.

The DUNES survey results provide a legacy value useful to the broad community, accomplishing in that way one of the rules for *Herschel* key programmes.

References

Allen, D. A., & Cragg, T. A. 1983, MNRAS, 203, 777

Augereau, J. C., Nelson, R. P., Lagrange, A. M., Papaloizou, J. C. B., & Mouillet, D. 2001, A&A, 370, 447

Aumann, H. H., & Probst, R. G. 1991, ApJ, 368, 264

Aumann, H. H., Beichman, C. A., Gillett, F. C., et al. 1984, ApJ, 278, L23

Avrett, E. H. 2003, in Current Theoretical Models and Future High Resolution Solar Observations: Preparing for ATST, eds. A. A. Pevtsov, & H. Uitenbroek, ASP Conf. Ser., 286, 419

Bach, K., Lee, J., Demarque, P., & Kim, Y.-C. 2009, ApJ, 703, 362

Backman, D. E., & Paresce, F. 1993, in Protostars and Planets III, eds. E. H. Levy, & J. I. Lunine, 1253

Backman, D. E., Dasgupta, A., & Stencel, R. E. 1995, ApJ, 450, L35

Bakos, G. Á., Sahu, K. C., & Németh, P. 2002, ApJS, 141, 187

Beichman, C. A., Bryden, G., Gautier, T. N., et al. 2005, ApJ, 626, 1061

Beichman, C. A., Bryden, G., Stapelfeldt, K. R., et al. 2006, ApJ, 652, 1674

Beichman, C. A., Lisse, C. M., Tanner, A. M., et al. 2011, ApJ, 743, 85

Berta, S., Magnelli, B., Lutz, D., et al. 2010, A&A, 518, L30

Berta, S., Magnelli, B., Nordon, R., et al. 2011, A&A, 532, A49

Bertone, E., Buzzoni, A., Chávez, M., & Rodríguez-Merino, L. H. 2004, AJ, 128, 829

Bonavita, M., & Desidera, S. 2007, A&A, 468, 721

Brott, I., & Hauschildt, P. H. 2005, in The Three-Dimensional Universe with Gaia, eds. C. Turon, K. S. O'Flaherty, & M. A. C. Perryman, ESA SP, 576, 565

Bryden, G., Beichman, C. A., Trilling, D. E., et al. 2006, ApJ, 636, 1098

Bryden, G., Beichman, C. A., Carpenter, J. M., et al. 2009, ApJ, 705, 1226

Carter, B. S. 1990, MNRAS, 242, 1

Castelli, F., & Kurucz, R. L. 2003, in Modelling of Stellar Atmospheres, eds. N. Piskunov, W. W. Weiss, & D. F. Gray, IAU Symp., 210, 20

Cox, A. N. 2000, Allen's astrophysical quantities

Decin, G., Dominik, C., Waters, L. B. F. M., & Waelkens, C. 2003, ApJ, 598, 636

Dohnanyi, J. S. 1969, J. Geophys. Res., 74, 2531

Dommanget, J., & Nys, O. 2002, VizieR Online Data Catalog, I/274

Donaldson, J. K., Roberge, A., Chen, C. H., et al. 2012, ApJ, 753, 147

Eggenberger, A., Udry, S., Chauvin, G., et al. 2007, A&A, 474, 273

Eggenberger, P., Miglio, A., Carrier, F., Fernandes, J., & Santos, N. C. 2008, A&A, 482, 631

Eiroa, C., Fedele, D., Maldonado, J., et al. 2010, A&A, 518, L131

Eiroa, C., Marshall, J. P., Mora, A., et al. 2011, A&A, 536, L4

Elias, J. H., Frogel, J. A., Matthews, K., & Neugebauer, G. 1982, AJ, 87, 1029

Elias, J. H., Frogel, J. A., Hyland, A. R., & Jones, T. J. 1983, AJ, 88, 1027

Ertel, S., Wolf, S., Metchev, S., et al. 2011, A&A, 533, A132

Ertel, S., Wolf, S., Marshall, J. P., et al. 2012a, A&A, 541, A148

Ertel, S., Wolf, S., & Rodmann, J. 2012b, A&A, 544, A61

ESA, ed. 1997, in The HIPPARCOS and TYCHO catalogues. Astrometric and photometric star catalogues derived from the ESA HIPPARCOS Space Astrometry Mission, ESA SP, 1200

Fischer, D. A., & Valenti, J. 2005, ApJ, 622, 1102

Flower, P. J. 1996, ApJ, 469, 355

Fruchter, A. S., & Hook, R. N. 2002, PASP, 114, 144

Fuhrmann, K. 2008, MNRAS, 384, 173

Gautier, III, T. N., Rieke, G. H., Stansberry, J., et al. 2007, ApJ, 667, 527

Ghezzi, L., Cunha, K., Smith, V. V., et al. 2010, ApJ, 720, 1290

Glass, I. S. 1975, MNRAS, 171, 19P

Gray, R. O., Corbally, C. J., Garrison, R. F., McFadden, M. T., & Robinson, P. E. 2003, AJ, 126, 2048

Gray, R. O., Corbally, C. J., Garrison, R. F., et al. 2006, AJ, 132, 161

Greaves, J. S., Fischer, D. A., Wyatt, M. C., Beichman, C. A., & Bryden, G. 2007, MNRAS, 378, L1

Griffin, M. J., Abergel, A., Abreu, A., et al. 2010, A&A, 518, L3

Gustafsson, B., Edvardsson, B., Eriksson, K., et al. 2008, A&A, 486, 951

Habing, H. J., Dominik, C., Jourdain de Muizon, M., et al. 2001, A&A, 365, 545

Halbwachs, J. L., Mayor, M., Udry, S., & Arenou, F. 2003, A&A, 397, 159

Hillenbrand, L. A., Carpenter, J. M., Kim, J. S., et al. 2008, ApJ, 677, 630

Holmberg, J., Nordström, B., & Andersen, J. 2009, A&A, 501, 941

Jewitt, D., Moro-Martìn, A., & Lacerda, P. 2009, The Kuiper Belt and Other Debris Disks, eds. H. A. Thronson, M. Stiavelli, & A. Tielens, 53

Kennedy, G. M., Wyatt, M. C., Sibthorpe, B., et al. 2012, MNRAS, 426, 2115

Koerner, D. W., Kim, S., Trilling, D. E., et al. 2010, ApJ, 710, L26

Koornneef, J. 1983, A&AS, 51, 489

Kóspál, Á., Ardila, D. R., Moór, A., & Ábrahám, P. 2009, ApJ, 700, L73

Krivov, A. V. 2010, Res. Astron. Astrophys., 10, 383

Krivov, A., Eiroa, C., Löhne, T., et al. 2013, ApJ, submitted

Lagrange, A.-M., Bonnefoy, M., Chauvin, G., et al. 2010, Science, 329, 57

Lawler, S. M., Beichman, C. A., Bryden, G., et al. 2009, ApJ, 705, 89

Liseau, R., Eiroa, C., Fedele, D., et al. 2010, A&A, 518, L132

Liseau, R., Montesinos, B., Olofsson, G., et al. 2013, A&A, 549, L7

Löhne, T., Augereau, J.-C., Ertel, S., et al. 2012, A&A, 537, A110

Luhman, K. L., Patten, B. M., Marengo, M., et al. 2007, ApJ, 654, 570

Luyten, W. J. 1979, LHS catalogue. A catalogue of stars with proper motions exceeding 0"5 annually

Maldonado, J., Martínez-Arnáiz, R. M., Eiroa, C., Montes, D., & Montesinos, B. 2010, A&A, 521, A12

Maldonado, J., Eiroa, C., Villaver, E., Montesinos, B., & Mora, A. 2012, A&A, 541, A40

Mamajek, E. E., & Hillenbrand, L. A. 2008, ApJ, 687, 1264

Marshall, J. P., Löhne, T., Montesinos, B., et al. 2011, A&A, 529, A117

Martínez-Arnáiz, R., Maldonado, J., Montes, D., Eiroa, C., & Montesinos, B. 2010, A&A, 520, A79

Mason, B. D., Wycoff, G. L., Hartkopf, W. I., Douglass, G. G., & Worley, C. E. 2011, VizieR Online Data Catalog, II/026

Matthews, B. C., Sibthorpe, B., Kennedy, G., et al. 2010, A&A, 518, L135

Mayor, M., Marmier, M., Lovis, C., et al. 2011, A&A, submitted [arXiv:1109.2497]

Moór, A., Ábrahám, P., Derekas, A., et al. 2006, ApJ, 644, 525

Moór, A., Pascucci, I., Kóspál, Á., et al. 2011, ApJS, 193, 4

Moro-Martín, A., & Malhotra, R. 2005, ApJ, 633, 1150

Moro-Martín, A., Carpenter, J. M., Meyer, M. R., et al. 2007, ApJ, 658, 1312

Mouillet, D., Larwood, J. D., Papaloizou, J. C. B., & Lagrange, A. M. 1997, MNRAS, 292, 896

Mustill, A. J., & Wyatt, M. C. 2009, MNRAS, 399, 1403

Ott, S. 2010, in Astronomical Data Analysis Software and Systems XIX, eds. Y. Mizumoto, K.-I. Morita, & M. Ohishi, ASP Conf. Ser., 434, 139

Phillips, N. M., Greaves, J. S., Dent, W. R. F., et al. 2010, MNRAS, 403, 1089

Pilbratt, G. L., Riedinger, J. R., Passvogel, T., et al. 2010, A&A, 518, L1

Poglitsch, A., Waelkens, C., Geis, N., et al. 2010, A&A, 518, L2

Pourbaix, D., Tokovinin, A. A., Batten, A. H., et al. 2004, A&A, 424, 727

Quillen, A. C., & Thorndike, S. 2002, ApJ, 578, L149

Rieke, G. H., Su, K. Y. L., Stansberry, J. A., et al. 2005, ApJ, 620, 1010

Rodriguez, D. R., & Zuckerman, B. 2012, ApJ, 745, 147

Santos, N. C., Israelian, G., & Mayor, M. 2004, A&A, 415, 1153

Selby, M. J., Hepburn, I., Blackwell, D. E., et al. 1988, A&AS, 74, 127

Sibthorpe, B., Ivison, R. J., Massey, R. J., et al. 2012, MNRAS, L3

Skiff, B. A. 2009, VizieR Online Data Catalog, II/023

Smith, B. A., & Terrile, R. J. 1984, Science, 226, 1421

Sousa, S. G., Santos, N. C., Mayor, M., et al. 2008, A&A, 487, 373

Su, K. Y. L., Rieke, G. H., Stansberry, J. A., et al. 2006, ApJ, 653, 675

Takeda, Y., Ohkubo, M., Sato, B., Kambe, E., & Sadakane, K. 2005, PASJ, 57, 27

Tanner, A., Beichman, C., Bryden, G., Lisse, C., & Lawler, S. 2009, ApJ, 704, 109
Thebault, P., Kral, Q., & Ertel, S. 2012, A&A, 547, A92
Trilling, D. E., Stansberry, J. A., Stapelfeldt, K. R., et al. 2007, ApJ, 658, 1289
Trilling, D. E., Bryden, G., Beichman, C. A., et al. 2008, ApJ, 674, 1086
Valenti, J. A., & Fischer, D. A. 2005, ApJS, 159, 141
van Leeuwen, F. 2007, A&A, 474, 653
van Leeuwen, F. 2008, VizieR Online Data Catalog, I/311
Vitense, C., Krivov, A. V., & Löhne, T. 2010, A&A, 520, A32
Vitense, C., Krivov, A. V., Kobayashi, H., & Löhne, T. 2012, A&A, 540, A30
Wright, C. O., Egan, M. P., Kraemer, K. E., & Price, S. D. 2003, AJ, 125, 359
Wyatt, M. C. 2008, ARA&A, 46, 339
Wyatt, M. C., Kennedy, G., Sibthorpe, B., et al. 2012, MNRAS, 424, 1206

[1] Universidad Autónoma de Madrid, Dpto. Física Teórica, Módulo 15, Facultad de Ciencias, Campus de Cantoblanco, 28049 Madrid, Spain

[2] ESA-ESAC Gaia SOC, PO Box 78, 28691 Villanueva de la Cañada, Madrid, Spain

[3] Centro de Astrobiología (INTA-CSIC), ESAC Campus, PO Box 78, 28691 Villanueva de la Cañada, Madrid, Spain

[4] Institut d'Astrophysique et de Géophysique, Université de Liège, 17 Allée du Six Août, 4000 Sart Tilman, Belgium

[5] UJF-Grenoble 1/CNRS-INSU, Institut de Planétologie et d'Astrophysique de Grenoble (IPAG), UMR 5274, 38041 Grenoble, France

[6] European Space Observatory, Alonso de Cordova 3107, Vitacura Casilla 19001, Santiago 19, Chile

[7] Max-Planck Institut für Astronomie, 69117 Königstuhl, Germany

[8] Jet Propulsion Laboratory, California Institute of Technology, 4800 Oak Grove Drive, Pasadena, CA 91109, USA

[9] NASA Goddard Space Flight Center, Exoplanets and Stellar Astrophysics, Code 667, Greenbelt, MD 20771, USA

[10] Instituto Nacional de Astrofísica, Optica y Electrónica, Luis Enrique Erro 1, Sta. Ma. Tonantzintla, Puebla, México

[11] ESA Astrophysics & Fundamental Physics Missions Division, ESTEC/SRE-SA, Keplerlaan 1, 2201 AZ Noordwijk, The Netherlands

[12] Astrophysikalisches Institut und Universitätssternwarte, Friedrich-Schiller-Universität, Schillergäßchen 2-3, 07745 Jena, Germany

[13] Department of Earth and Space Sciences, Chalmers University of Technology, Onsala Space Observatory, SE-439 92 Onsala, Sweden

[14] Georg-August-Universität Göttingen, Institut für Astrophysik, Friedrich-Hund-Platz 1, 37077 Göttingen, Germany

[15] LESIA, Observatoire de Paris, 92195 Meudon, France

[16] Christian-Albrechts-Universität zu Kiel, Institut für Theoretische Physik und Astrophysik, Leibnizstr. 15, 24098 Kiel, Germany

[17] NASA Herschel Science Center, California Institute of Technology, 1200 E. California Blvd., Pasadena, CA 91125, USA

[18] NASA ExoPlanet Science Institute, California Institute of Technology, 1200 E. California Blvd., Pasadena, CA 91125, USA

[19] ISDEFE at ESAC, 28691 Villanueva de la Cañada, Madrid, Spain

[20] Universidad Complutense de Madrid, Facultad de Ciencias Físicas, Dpt. Astrofísica, av. Complutense s/n, 28040 Madrid, Spain

[21] Department of Astronomy, Stockholm University, AlbaNova University Center, Roslagstullsbacken 21, 106 91 Stockholm, Sweden

[22] Steward Observatory, University of Arizona, 933 North Cherry Avenue, Tucson, AZ 85721, USA

[23] Rutherford Appleton Laboratory, Chilton OX11 0QX, UK

[24] Department of Physics and Astrophysics, Open University, Walton Hall, Milton Keynes MK7 6AA, UK

[25] Calar Alto Observatory, Centro Astronómico Hispano-Alemán, c/ Jesús Durbán Remón, 2-2, 04004 Almería, Spain

[26] Nagoya University, Japan

[27] Max-Planck-Institut für Kernphysik, Saupfercheckweg 1, 69117 Heidelberg, Germany

[28] Kapteyn Astronomical Institute, Postbus 800, 9700 AV Groningen, The Netherlands

[29] Herschel Science Center, ESAC/ESA, PO Box 78, 28691 Villanueva de la Cañada, Madrid, Spain

[30] Observatoire de la Côte d'Azur, Boulevard de l'Observatoire, BP 4229, 06304 Nice Cedex 4, France

[31] Institute of Space and Astronautical Science (ISAS), Japan Aerospace Exploration Agency (JAXA), 3-1-1, Yoshinodai, Chuo-ku, Sagamihara, 252-5210 Kanagawa, Japan

[32] Institut de Ciències de l'Espai (CSIC-IEEC), Campus UAB, Facultat de Ciències, Torre C5, parell, 2a pl., 08193 Bellaterra, Barcelona, Spain

[33] ESA-ESAC, Science Archives Team, PO Box 78, 28691 Villanueva de la Cañada, Madrid, Spain

Appendix A: DUNES Virtual Observatory tool

The achievement of the DUNES objectives requires a detailed knowledge of the properties and environment of the targets to be studied. There exists a huge amount of astrophysical data and information about the DUNES objects, distributed in a number of archives and services. Gathering information in a wide variety of types and formats from a large number of heterogeneous astronomical data services is a tedious, very time consuming task even for a modest data set. With this aim we have developed a Virtual Observatory[11] (VO) application for accessing, visualizing and downloading the information on DUNES targets available in astronomical archives and services. Given a list of objects, identified by their names or coordinates, a real-time exploration of Vizier[12] using VO protocols is performed to gather photometric data as well as physical parameters. This information can be complemented with searches of images, spectra and catalogues in all the Virtual Observatory services. Moreover, ad hoc access to other non VO-compliant services of interest (like NStED or *Spitzer*/FEPS) is also provided. The obtained information can be downloaded in ASCII, VOTable (standard format for tabular data in the Virtual Observatory) or HTML format. For heavy queries, the tool implements a batch mode informing the user via e-mail when the search is complete. The message includes a link to the data through which the information can be downloaded.

In addition, one of the goals of the DUNES consortium is to provide the astronomical community with a legacy VO-compliant archive, as also requested by rules of the *Herschel* OTKPs. The DUNES Archive System[13] is designed to ensure that other research groups gain easy access to both *Herschel* reduced data and ancillary data (photometry and physical parameters gathered from VO services), as well as to the DUNES VO discovery tool, the DUNES project web page as well as to a section including news on the archive. A HelpDesk to pose questions to archive staff is also available.

Appendix B: Stellar fluxes and parameters

Table 3, with several subtables, presents the magnitudes and fluxes of the DUNES stars which have been used to trace their spectral energy distributions. Optical, near-IR, WISE, AKARI, IRAS and *Spitzer* data are included.

Table 4 gives some relevant parameters of the stars. $T_{\rm eff}$, $\log g$ and [Fe/H] are average values of photometric and spectroscopic estimates mainly from Gray et al. (2003); Santos et al. (2004); Takeda et al. (2005); Valenti & Fischer (2005); Gray et al. (2006); Fuhrmann (2008); Sousa et al. (2008); Holmberg et al. (2009). Rotational velocity values are taken from Martínez-Arnáiz et al. (2010). Bolometric luminosities and stellar radii have been estimated from the absolute magnitudes and bolometric corrections using the measurements by Flower (1996). The activity index $\log R'_{\rm HK}$ has been taken from Martínez-Arnáiz et al. (2010) while we have derived the X-ray luminosities based on ROSAT, XMM and *Chandra* data. The table also provides ages based on the $\log R'_{\rm HK}$ index and on the X-ray luminosities as estimated by Maldonado et al. (2010). There is a wide range of age estimates in the literature using

different tracers for the DUNES stars. Stellar ages of our targets are difficult to estimate on the basis of isochrones given that the stars are located on the main-sequence (see Fig. 2) and that they are sensitive to $T_{\rm eff}$ and metallicity (Holmberg et al. 2009). Thus, we have opted to give in Table 4 the age estimates based on our own coherent data set and procedure.

Appendix C: Prediction of photospheric fluxes at the PACS and SPIRE wavelengths

C.1. Models

The behaviour of three families of model atmospheres was studied in order to choose the best option for the photospheric work of the project: PHOENIX/GAIA (Brott & Hauschildt, 2005), ATLAS9 (Castelli & Kurucz 2003) and MARCS (Gustafsson et al. 2008). It was found that for $T_{\rm eff} \geq 5000$ K the three sets of models are virtually identical. In the interval 4000–5000 K the models start to show some differences which are more pronounced towards lower temperatures and shorter wavelengths, the models being identical for $\lambda > 4$ μm. For lower temperatures – only seven DUNES stars have $T_{\rm eff}$ below 4000 K – the three sets of models present larger discrepancies, with ATLAS9 being more different when compared with the other two families.

The PHOENIX/GAIA set of models was finally chosen because of its finer grid in effective temperatures, sampling of the individual model spectra and overall behaviour. The models were computed in LTE, the opacity treated with the opacity sampling formalism, and more than 300 million lines were included. The synthetic spectra have a variable amount of wavelength points, between 50 000 and 55 000, cover the interval 0.001–50 μm, $v_{\rm turb}$ was set to 2 km s^{-1}, the mixing length parameter is 1.5 and the geometry is plane parallel, or spherical in those cases where that one is not correct.

Due to their extremely large resolution, the synthetic spectra were smoothed with a Gaussian filter with $FWHM = 0.005$ after taking the decimal logarithm of the wavelengths in angstroms. Following that, the wavelength scale was put back in physical units.

A grid of 1980 spectra (55 temperatures ×6 gravities ×6 metallicities) was available. The ranges covered are 3000 K $< T_{\rm eff} <$ 9800 K, 3.0 $< \log g <$ 5.5 (step 0.5 dex) and $-2.0 <$ [Fe/H] $< +0.5$ (step 0.5 dex).

In general, the synthetic spectrum for a given star is not contained in the grid, therefore, an interpolation in three dimensions had to be done. Since the PHOENIX/GAIA models only run up to $\lambda = 40$ μm, an extension up to 4 mm using the Rayleigh-Jeans approximation was attached to the original model.

C.2. Normalization of the models to the observed SED

The normalization of the model photosphere to the observed SED was done using the procedure outlined by Bertone et al. (2004). The monochromatic fluxes of the SED, $s(\lambda)$ (in units of Jy), were compared with those of the synthetic model, $m(\lambda)$ (in the same units), at the corresponding wavelengths, deriving a residual function:

$$X(\lambda_{\rm i}) = \ln s(\lambda_{\rm i}) - \ln m(\lambda_{\rm i}) + k. \tag{C.1}$$

The offset constant is such that

$$\sum_{\rm i} X(\lambda_{\rm i}) = 0 \tag{C.2}$$

so $k = \langle \ln m(\lambda) - \ln s(\lambda) \rangle$.

---

[11] The VO is a project designed to provided the astronomical community with the data access and the research tools necessary to enable the exploration of the digital, multi-wavelength universe resident in the astronomical data archives. http://www.ivoa.net

[12] http://vizier.u-strasbg.fr/cgi-bin/VizieR

[13] http://sdc.cab.inta-csic.es/dunes

Five subsets of the full SED were chosen to carry out five normalizations, namely, VI+nIR, BVI+nIR, VI+nIR+WISE, nIR+WISE and VI+nIR+WISE. The near infrared photometry (nIR) consists of 2MASS JHK_s (only magnitudes with quality flags "A" or "B" were considered), plus additional JHKL points, when available. WISE band W1 (3.35 μm) was used in most of the cases despite of being nominally saturated[14] because PSF photometry was carried out on the images and therefore the values provided in the all-sky release turned out to be usable (Stapelfeldt, priv. comm.), only the brightest targets showed unacceptable values of W1 magnitudes; WISE W2 (4.60 μm) photometry was never used; its flux level, when looking at the SED as a whole, always deviates from the overall behaviour; WISE W3 (11.56 μm) was always used unless it was brighter than the saturation magnitude; WISE W4 (22.09 μm) was also always used unless the shape of the SED indicated that an excess could start around that wavelength.

Since each normalization was done with a different number of points (e.g. degrees of freedom), a reduced χ^2 was computed for each one in order to make a comparison of all of them. The selected normalization was that with the least reduced χ^2 and was used to predict the fluxes at the PACS and SPIRE wavelengths. The uncertainties in the individual photospheric fluxes were estimated by computing the total σ of the normalization, in logarithmic units; in this calculation the observed flux at each wavelength involved in the normalization process was compared with its corresponding predicted flux. The result is that the normalized model log $S(\lambda)$ can be allowed to move up and down a quantity $\pm\sigma$. That value of σ was then translated into individual – linear – uncertainties of the fluxes at the relevant *Herschel* wavelengths.

Appendix D: Spurious sources

There is a number of objects whose fluxes seemingly denote an excess, which can in a first instance be attributed to a circumstellar disc, but whose morphologies and surrounding fields suggest they are not true debris discs associated with the stars. Very likely, these stars are affected by coincidental alignment or contamination from a structured background. In the following, we briefly describe these cases and show their PACS images and contour plots in Figs. D.1 and D.2. Table D.1 lists these sources

together with their PACS and predicted photospheric fluxes. The significance of the "apparent" excesses is also given, as well as the *Spitzer* MIPS 70 μm fluxes.

HIP 29568. The 160 μm flux has a significance of $\chi_{160} = 3.00$ (Table D.1), being a cold disc candidate. However, the image shows a lot of background structure (Fig. D.1) which makes the flux estimate doubtful.

HIP 38784. This is a faint star which apparently shows a small excess at 160 μm. However, reduced images from HIPE versions 7.2 (Fig. D.1) and 4.2 are not quite consistent, as neither are the individual scans likely due to the faintness of the source.

HIP 40843. This star was identified by *Spitzer* as an excess source. However, the positional offset between the star and the peak of the PACS image is large. Both the 100 and 160 μm images are extended but practically in perpendicular directions (Fig. D.1). The fluxes of the table correspond to the whole extended emission. However, given the position of the star and the different orientations at 100 and 160 μm, we consider it a case of coincidental alignment of a background galaxy. In fact, there is a very faint, secondary 100 μm peak embedded in the extended emission. This peak is at the position α (2000.0) = 8:20:03.78, δ (2000.0) = 27:13:4.6, i.e., and offset of 1''4 wrt the optical positions on the star, and of 8''1 wrt the main 100 μm peak. A 2D Gaussian fit supports the presence of two peaks.

HIP 71908. The star lies on top of an emission strip at both 100 and 160 μm (Fig. D.2), which prevents us from estimating an enough accurate flux in the red band. This star is located at the galactic plane. The marginal 100 μm significance, $\chi 100 = 3.13$, is likely not real.

HIP 85295. There is an offset between the 100 μm peak, which coincides with the optical position, and the 160 μm peak emission (Fig. D.2). At this wavelength, the object seems to be formed by two different ones separated by ~6''. The western one is close to the 100 μm peak. Thus, the apparent excess emission at 160 μm is likely due to contamination by a background galaxy.

HIP 105312. The 100 μm peak agrees well with the optical position, but the 160 μm emission, which appears resolved, is displaced a bit towards the west. (Fig. D.2).

HIP 113576. This is a case of a very clear offset between the 100 and the 160 μm emission, which likely falsifies the presence of an excess (Fig. D.2).

Table D.1. DUNES stars whose apparent excesses are very likely due to contamination by background galactic extended structures or extragalactic objects.

HIP	SpT	PACS70 (mJy)	S70 (mJy)	χ_{70}	PACS100 (mJy)	S100 (mJy)	χ_{100}	PACS160 (mJy)	S160 (mJy)	χ_{160}	MIPS70 (mJy)
29568	G5V		10.48 ± 0.19		7.83 ± 1.16	5.13 ± 0.10	1.92	8.28 ± 2.11	2.01 ± 0.04	3.00	15.3 ± 2.3
38784	G8V	8.66 ± 2.65	9.47 ± 0.10	−0.31	4.19 ± 0.74	4.64 ± 0.05	−0.61	5.98 ± 1.28	1.81 ± 0.02	3.26	10.6 ± 3.0
40843	F6V		22.59 ± 0.13		33.17 ± 2.76	11.07 ± 0.06	8.03	53.35 ± 3.17	4.32 ± 0.02	15.47	32.5 ± 5.3
71908	F1Vp		68.58 ± 4.16		38.54 ± 1.58	33.60 ± 2.04	3.13		13.13 ± 0.80		
85295	K7V		21.14 ± 0.46		12.94 ± 1.12	10.36 ± 0.22	2.30	14.15 ± 3.29	4.05 ± 0.09	3.07	13.8 ± 4.6
105312	G5V	12.44 ± 1.72	11.86 ± 0.66	0.34	7.84 ± 0.76	5.81 ± 0.32	2.67	9.20 ± 1.74	2.27 ± 0.13	3.98	13.6 ± 5.7
113576	K5/M0V		19.01 ± 0.97		9.43 ± 0.79	9.32 ± 0.48	0.14	12.66 ± 1.50	3.64 ± 0.19	6.01	19.1 ± 2.9

Notes. PACS and predicted photospheric fluxes, and the significance of the measured apparent excesses are given. The last column gives *Spitzer* MIPS fluxes at 70 μm.

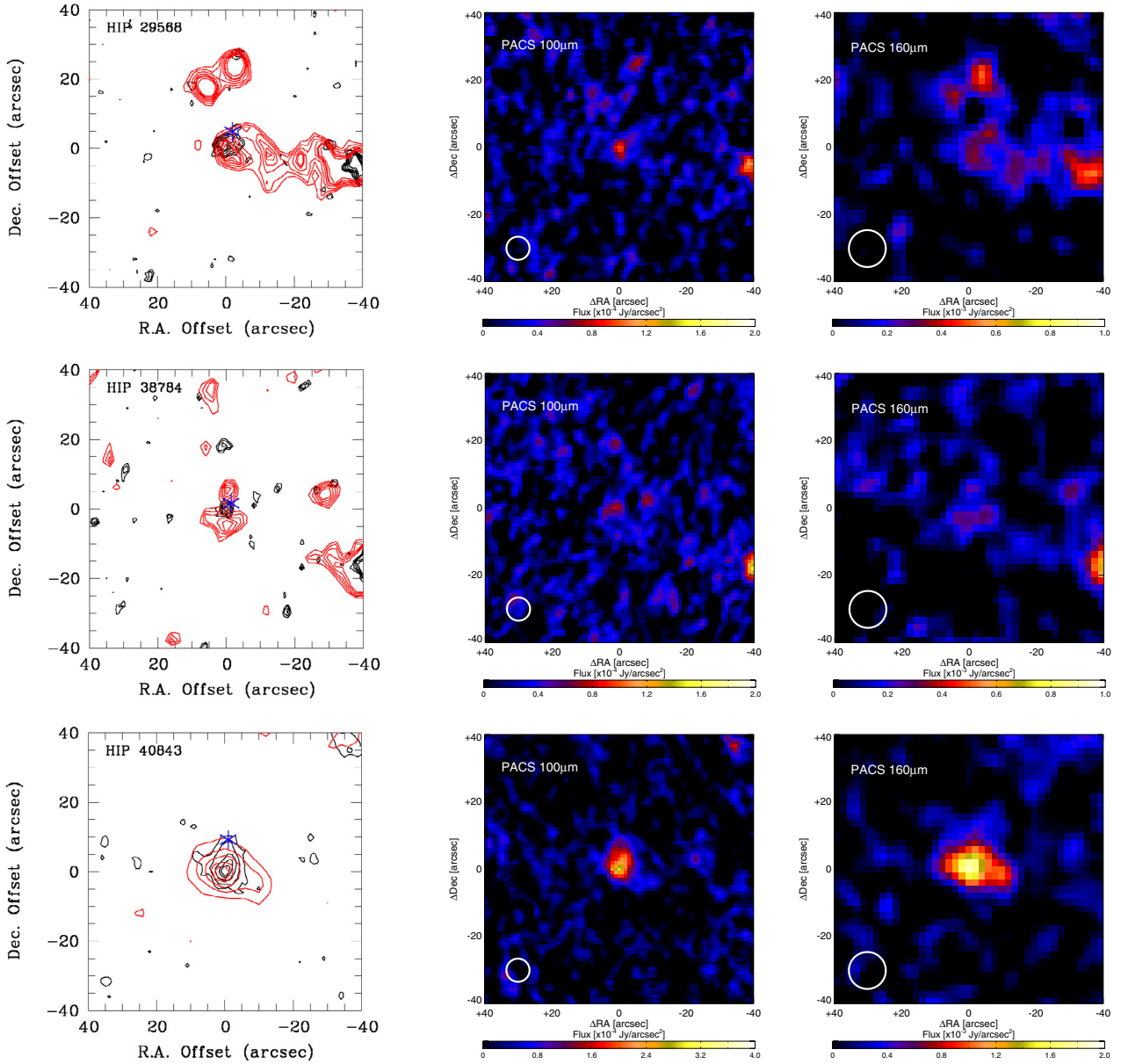[14] http://wise2.ipac.caltech.edu/docs/release/allsky/expsup/sec6_3d.html

Fig. D.1. Contour plots (*left*) and PACS 100 μm (*middle*) and 160 μm (*right*) images of stars for which contamination impacts the apparent excesses of the stars. The identification of the stars are given in the upper-left corner of the contour plots. Position (0,0) refers to the 100 μm peak. The optical position of the stars with respect to the 100 μm peak is indicated by a "star" symbol. North is up and east to the left. Black contours correspond to 100 μm and red contours to 160 μm. HIP 29568: contours are 40%, 50%, 60%, 70%, 80%, 90% of the peak at both bands. HIP 38784: contours are 50%, 60%, 70%, 80%, 90% of the peak at both bands. HIP 40843: contours 20%, 40%, 60%, 80%, 90% of the peak at both bands.
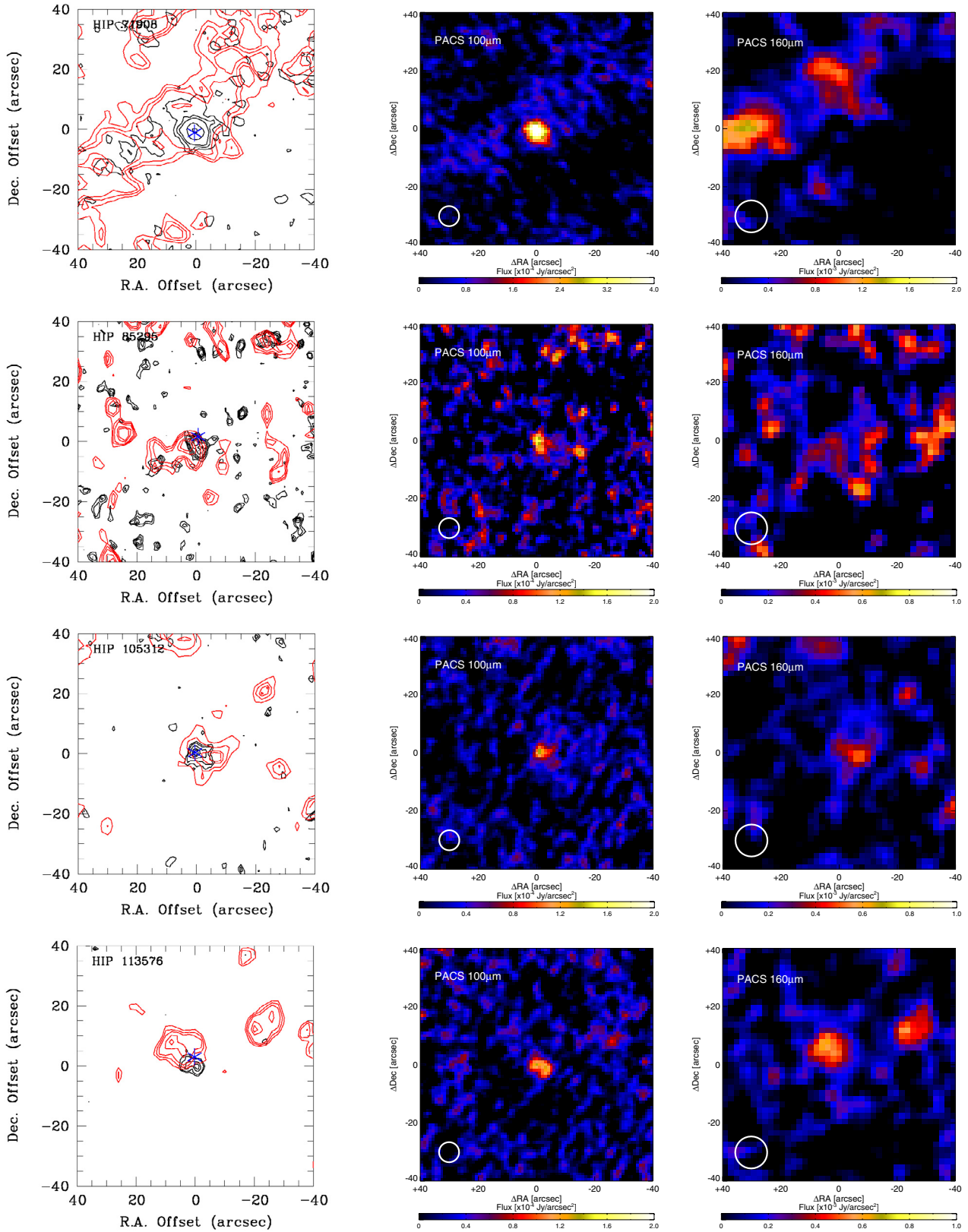
Fig. D.2. Same as Fig. D.1. In this case contours are 20%, 40%, 60%, 80%, 90% of the peak at both 100 and 160 μm bands for all the images.
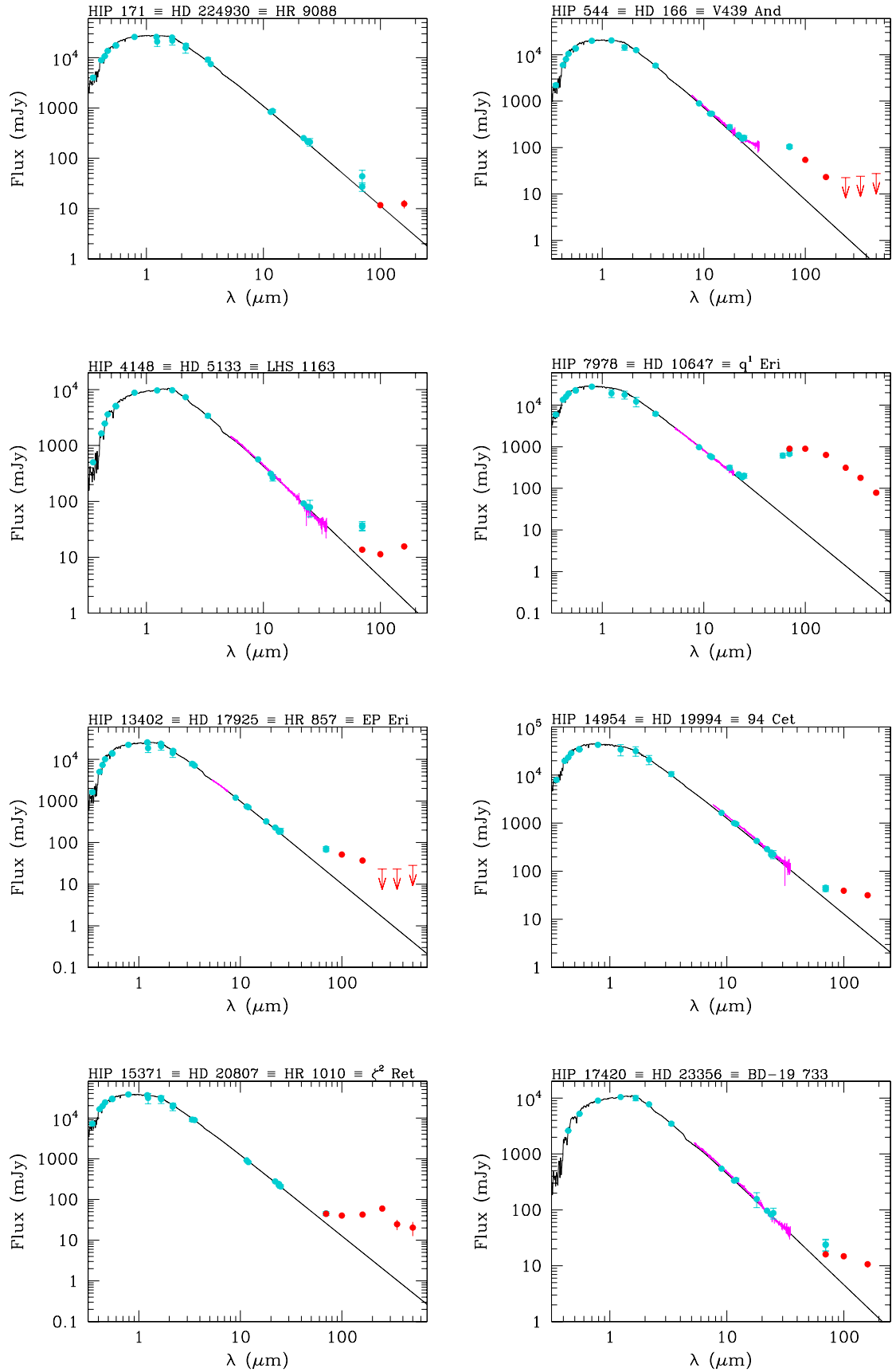
Appendix E: SEDs of the excess sources

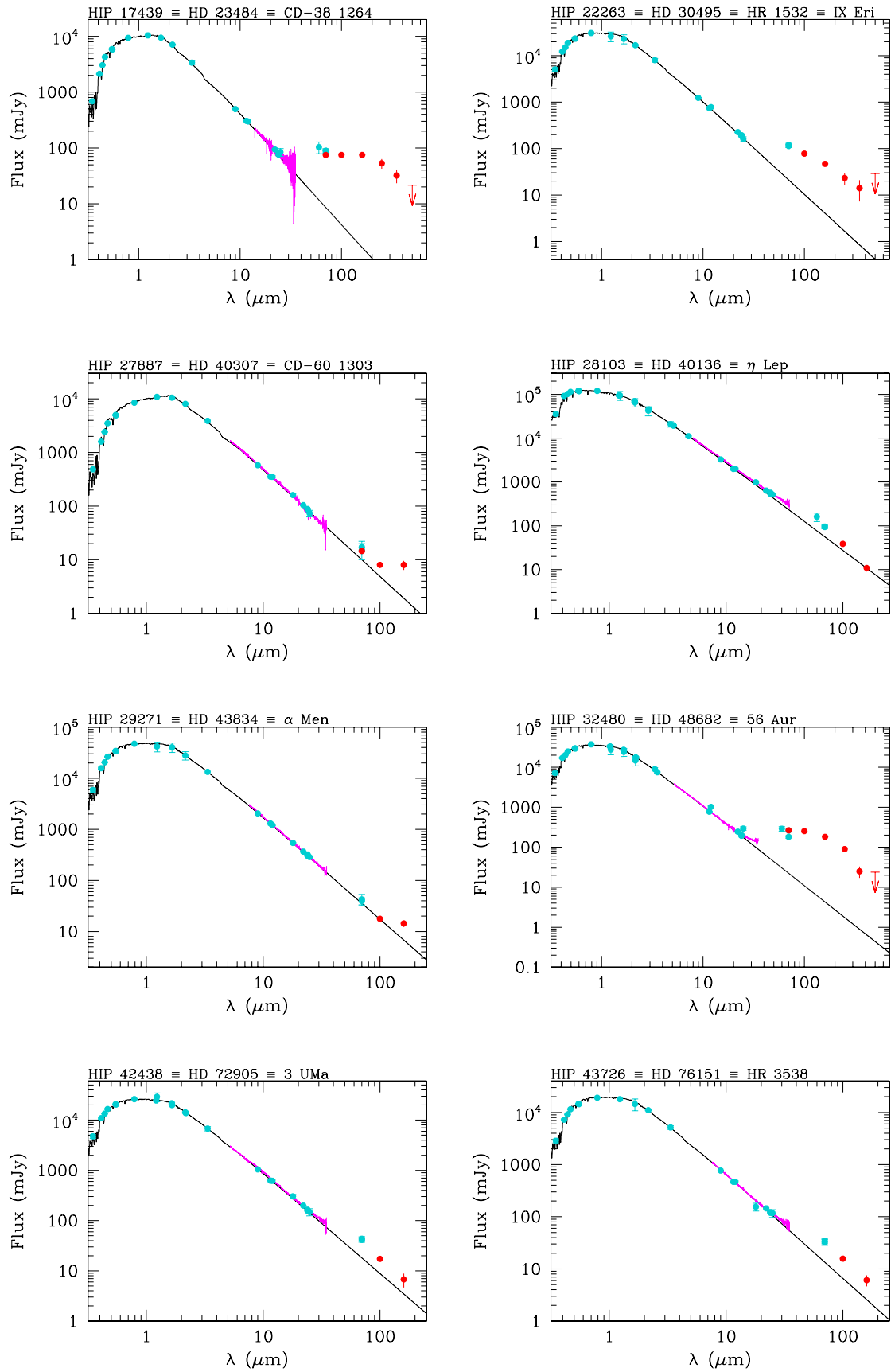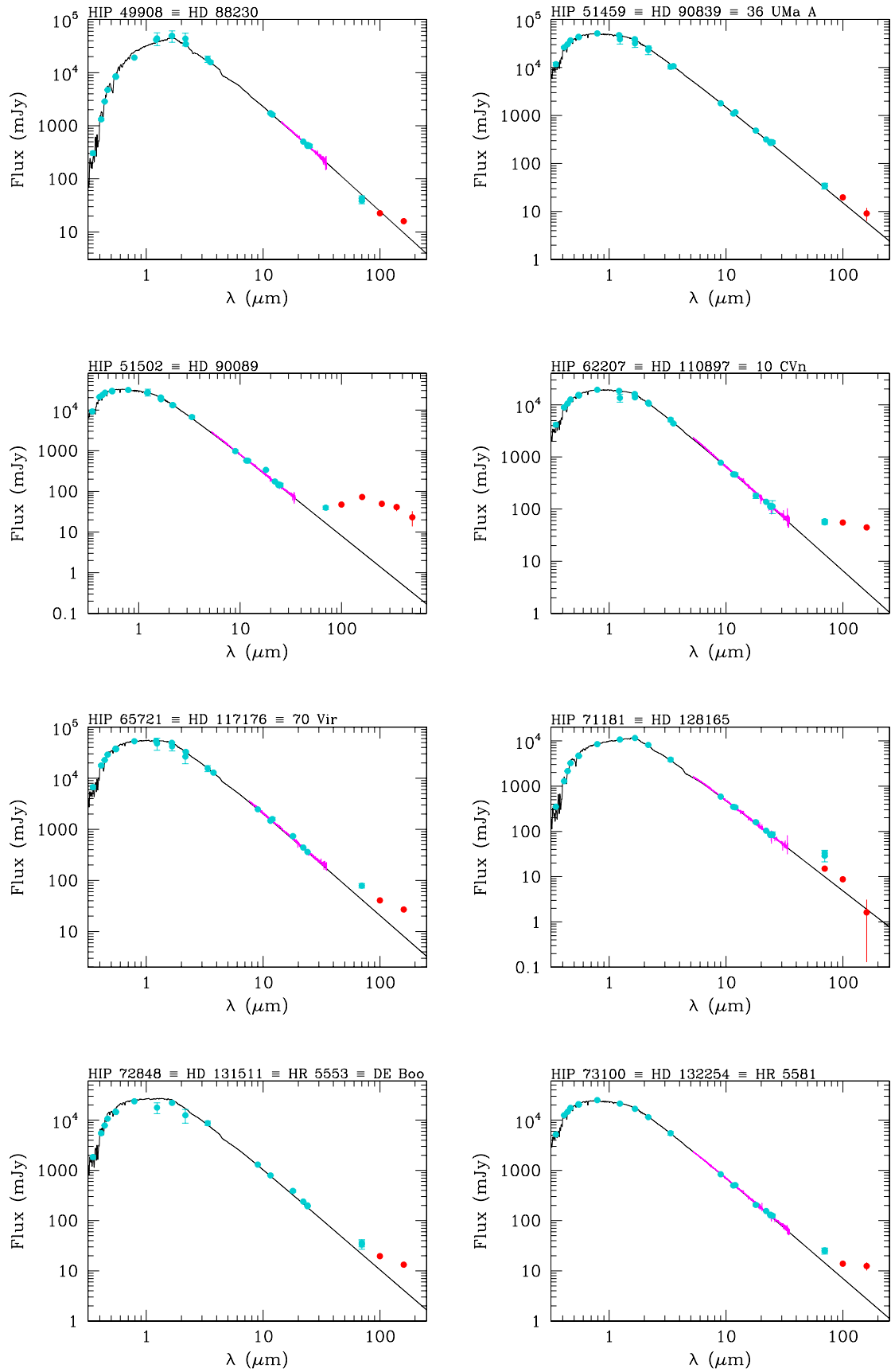**Fig. E.1.** SEDs of DUNES stars with excesses.

Fig. E.1. continued.

Fig. E.1. continued.

Fig. E.1. continued.